NAGOYA UNIVERSITY

DOCTORAL THESIS

Plasma Simulation Analysis for Formation Mechanism of Periodic Nanograting Structures by Laser Pulses

---

Author:

Amany Moustafa **Gouda**

Supervisor:

Professor Hitoshi Sakagami

A thesis submitted in fulfillment of the requirements

for the degree of Doctor of Science

in the

ΣT Laboratory

Astrophysics and Particle Physics Department

October 2018

Declaration of Authorship

I am, Amany Moustafa Gouda, declare that this thesis titled, ' Plasma Simulation Analysis for Formation Mechanism of Periodic Nanograting Structures by Laser Pulses' and the work presented in it is my the intellectual property of mine under the supervision of Professor Sakagami. I confirm that:

- This work was done wholly or mainly while in candidature for a research degree at this University.

- Where any part of this thesis has previously been submitted for a degree or any other qualification at this university or any other institution, this has been clearly stated.

- Where I have consulted the published work of others, this is always clearly attributed.

- Where I have quoted from the work of others, the source is always given. With the exception of such quotations, this thesis is entirely my own work.

- I have acknowledged all main sources of help.

- Where the thesis is based on work done by myself jointly with others, I have made clear exactly what was done by others and what I have contributed myself.

Signed:

_____

Date:

_____

"All people have their own exams, even ants have their exams."

Mom

Abstract

Many laser experiments report that repeated irradiation of ultrahigh intensity short pulse lasers can self-organizationally form periodic nanograting structures, whose interspace is less than the laser wavelength, on material surfaces even any perturbations as a seed for such structures do not exist. The formation mechanisms of such structures were suggested, but they are still not verified due to difficulty in temporal-spatial resolved measurements and it is not fully understood yet. On the other hand, as the laser fluence must be greater than the ablation threshold to form the structure, interactions between the laser and ablation plasmas could play an important role in the formation. Therefore, two-dimensional relativistic electromagnetic Particle-In-Cell code is used to simulate laser-plasma interactions and investigate the formation mechanism of the periodic nanograting structure.

In the case of relativistic laser intensity, high density plasma with 10 times critical density is assumed as the target and under critical density plasma is placed in front of the target as ablated plasma. As a consequence of simulations, it is shown that small tips are periodically formed on the surface of high density plasma and they grow to form the periodic nanograting structure whose wavenumber vector is parallel to the laser polarization direction. Detail analysis of simulation data reveals that high energy electrons, that are generated by relativistic laser-plasma interactions, propagate into the high density plasma region, inducing the Weibel instability, and the typical Weibel structure of the electron current and the magnetic field leads to form the periodic nanograting structure.

When the target plasma is irradiated by the nonrelativistic intensity laser, the periodic nanograting structure with the shorter interspace than the laser wavelength is found on the expanded plasma surface which is diffused from the high density plasma even the Weibel instability is not induced due to low laser intensity. Using electron density profiles in simulations and the theoretical model, it is revealed that surface plasma waves are excited and propagate to upper and lower direction along the plasma surface, composing the standing wave, and small periodic perturbations are formed by the Ponderomotive force of this standing wave. As the plasma irradiated by the laser is under unstable conditions for the oscillating two-stream instability, those perturbations can grow and this situation is verified by theoretically evaluating the growth rate of the oscillating two-stream instability to be large enough to form the periodic nanograting structure in our case.

Acknowledgements

First and foremost, I want to thank Almighty Allah for giving me this chance by coming to this world and keeping me under his blessings throughout my life.

Secondly, I want to thank my supervisor, Professor Sakagami. It has been an honor to be his first international Ph.D. student. He has taught me how good simulation physics is done. I appreciate all his time, ideas, and funding to make my Ph.D. experience productive and stimulating. The joy and enthusiasm he has for his research were contagious and motivational for me, even during the tough times in the pursuit of my Ph.D. I am also thankful for the excellent example he has provided as a successful professor and researcher.

Lastly, I would like to thank my family members for all their love and encouragement. I want to thank my mother, who passed away in February 2018 before she could share my success. I want to thank my father, my brother, and my sister, who carried the responsibilities of my mother in her last days to give me a chance to continue my progress. Thank you all.

Amany Moustafa Gouda
September 2018

Contents

List of Figures

List of Tables

Chapter 1

Motivation and Outline

1.1 Motivation and background

Studying the nanostructure shows different linear optical properties and nonlinear optical properties in nano-composite materials [6]. Intensive theoretical, simulation and experimental studies for understanding the mechanism of formation the periodic nanograting structure have already published [7–9]. The generation of the periodic nanograting structures on metal surfaces after irradiating metal's surface with a laser beam in laboratories is still a kind of mystery in science and has been of much interest to the scientific community. Formation of the periodic nanograting structure can be considered as one type of the laser materials processing field which has a high intention especially after the laser got developed to a short pulses laser. Lasers used as one of an efficient and qualified tools for many application. The studying of the periodic nanograting structures and their formation mechanism are in continuous progress, the way of creating the periodic nanograting structure and how it grows up and reaches the stable level to be used in the industrial applications is one of the main worthwhile problems of modern science [10–12].

The researchers who tried to explain the formation of the periodic nanograting structure find that the creation of these structures in the different materials are relevant to some of the physical phenomena which were well understood in the early science steps. The electrostatic waves and the electromagnetic wave in the ionized medium can cause the periodic nanograting structure [9, 13]. The parametric instability and second harmonic generation are also used as other different physical phenomena to explain the formation mechanism [7, 11, 14]. Additional physical phenomena used to explain the formation mechanism, such as laser intensity modulation and excitation of Surface Plasmon Polarition model[7, 8].

Since 1999, self-organized periodic nanograting structures have been reported after irradiating the solid material surfaces with an ultrafast laser beam. Many researchers introduced the formation of periodic nanograting structures on surfaces of some material such as insulators [12, 15, 16], semiconductors [17], and metals [18, 19] as a way for advanced applications. Researchers show the orientation of the periodic structure is taking different direction whether perpendicular to the polarization direction of

the laser beam or parallel [11, 20]. As a result of getting self-organized periodic nanograting structures by using a laser beam, Many applications released in different fields such as functional biomaterials [21, 22], tribology for friction reduction [23, 24], protein folding [25], and metal coloring [26, 27]. Those previous applications show their results after irradiating material surfaces by laser beam. The laser beam has been considered as a leading tool for material processing such as drilling, grooving, and cutting into the metal [11]. Moreover, laser beam recorded wide applications in many other different fields of science not only precise material processing but also in nuclear fusion [28], medical surgery [29], photo-chemistry [30], laser scanner, surveying and ranging [31], images [32], and etc. Different laser types (picosecond, nanosecond, femtosecond) have been used in material processing field with different characteristic. For example, irradiation of material with nanosecond laser produces a heat zone transfer to the metal workpiece. Using of nanosecond laser leads to form molten metal, vapor, and plasma in a sequence leads to change of the structure morphology and limits the quality of the periodic structure that formed on the metal surfaces. considerable advantages for the periodic structure formation by using femtosecond laser in comparison with the nanosecond lasers [11]. The advantages of using femtosecond laser is based on rapid formation of plasma phase without passing on the liquid phase, such femtosecond laser characteristic will help to avoid the morphological damage. It was found that the periodic nanostructures lie whether perpendicular and/or parallel to the laser electric field while, in the simulations studies, the periodic structure is parallel to the polarization direction only [13, 20].

For further development of the periodic nanograting structure and their applications by using femtosecond laser, it is important to discuss some basic understanding to the formation mechanism of the periodic nanograting structure. The periodic structures can be divided into two types (i) resonant structures, this type of structure is correlated with laser wavelength. thus the so-called low spatially frequency LIPSS (LSFL) belongs to the resonant structures [7]. (ii) non-resonant structures, this type of structure are not correlated to both wavelength and the coherent of the femtosecond laser. In case of non-resonant structure of large size parallel ripples of several micrometers, many pulses are required to produce the structure. For femtosecond laser pulse, the production of plasma is still in close contact with the solid state matter. The plasma produced by laser expands at sonic speed $c_s = \sqrt{k_B T_e / M_i}$ (K_B, T_e, and M_i are the Boltzmann constant, the electron temperature, and the ion mass, respectively). The plasma scale length is of the order of $c_s \tau$ where τ is the pulse duration and it is sufficiently short to allow plasma to form a new surface formed from plasma. Therefore, the pulse can interact with the surface formed by plasma rather than with the bulk plasma.

Fig. 1.1 shows the repeated irradiation of short pulse lasers can form periodic nanostructure on a metal surface. The interspace of the copper thin film (solid circles) observed in the experiment [1] was in good agreement with the interspaces observed from the previous experiment (the open circles) for the same research group. The solid line is representing the results that have been calculated by using parametric decay model while the dotted line represents the direct calculation of the surface plasma
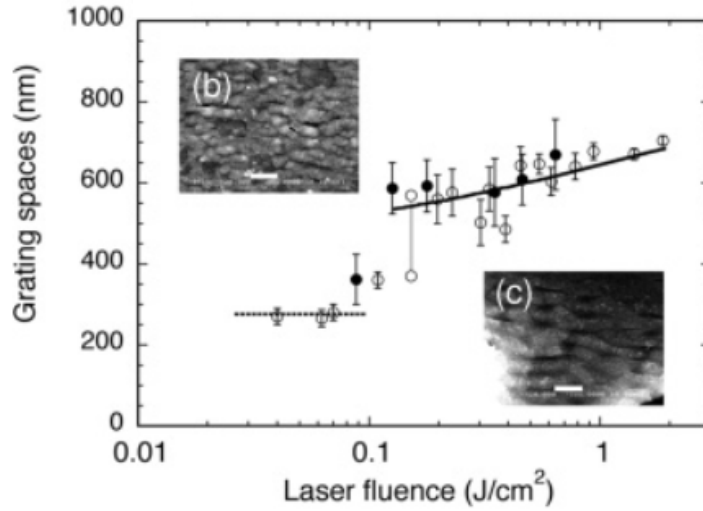
FIGURE 1.1: Shows the effect of the laser fluence J/cm^2 on the grating interspace nm in case of irradiating the copper thin film with the femtosecond laser beam of wavelength λ_L= 800 nm [1].

wave that produced directly by the laser. Surface morphologies of thin Cu films at laser fluences of (b) 0.089 J/cm^2 and (c) 0.35 J/cm^2 are shown. The scale bar in the photos corresponds to 1 μm.

1.2   Outline

This Ph.D. thesis can be considered as a simulation study for investigating the formation mechanism of periodic nanograting structures. Forming periodic nanograting structure is a one of the contemporary science issues that gained much attention in the last 20 years due to their vast usage in industrial applications. Our thesis presented two studied cases that contributed to explaining the formation mechanism. The first case aims to study the formation mechanism of the periodic nanograting structure by irradiating plasma with a laser beam of intensity 10^{18} W/cm^2-μm^2. The results of irradiating the plasma with relativistic laser beam show that Weibel instability can explain the formation mechanism within the relativistic regime of a laser beam. On the contrary, for the nonrelativistic laser beam, irradiating the plasma with a laser intensity of 10^{16} W/cm^2-μm^2 shows that the surface plasma wave (SPW) along with the oscillating two-stream (OTS) instability act as the formation mechanism for the second method.

The calculation of the formation mechanisms for creating periodic nanograting structures has been done using the particle in cell code (FISCOF2). The calculation of the interspace size and the accompanying plasma phenomena during the formation mechanism, such as magnetic field, electron current density, electric field, and electron density, were successfully investigated with the particle in cell code (FISCOF2).

This thesis contains five chapter used to explain our work. Chapter 1 provides a brief description of the motivation and background of our thesis. In chapter 1, the reader will get a summary of the other researcher work and some of the assumed models for studying the formation mechanism of periodic nanograting structure. Chapter 2 shows some basics of plasma physics science, which will help the reader to understand some basics of the thesis work.

Chapter 3 explains the mechanism of forming periodic nanograting structure by using FISCOF2 when the two regions of plasma interacting with the relativistic laser pulses of intensity $I = 10^{18}$ W/cm$^2 - \mu$m^2. We find a consistent between the z-component of the enhanced magnetic field B_z and x-component of the electron current density J_{xe} in forming the structure.

The Weibel instability theory has explained how the magnetic field is enhanced with time evolution and how the enhanced magnetic field share in forming the periodic structure. The Weibel instability can be considered as the first contribution to explain the periodic nanograting structure under effect of the relativistic laser beam. The structure has been observed as a self-organized structure along the boundary between the mimic-target plasma at t = 200 fs. The periodic nanograting structures at t = 250 fs is formed 13 tips along y-axis from -3.0 to 3.0 μm, the interspace size of 0.46 μm is shorter than the laser wavelength.

The periodic nanograting structures observed at y = -0.8, -0.6, -0.2, 0.3, and 0.9 μm in the electron density profile where the positive x-component of electron the current density J_{xe} exist. Furthermore, the positive and the negative z-component values of the enhanced magnetic field B_z are shown in between above positions. For example at y = 0.3 μm, the positive z-component of B_z exists at y = 0.5 μm while the negative z-component of B_z exists at y = 0.1 μm. The above description shows the consistence between the enhanced magnetic field and the electron current density which leads to producing periodic nanograting structure and confirm the existence of Weibel instability and its role in the formation mechanism.

In chapter 4, forming the periodic nanograting structures by nonrelativistic laser pulses has been studied by using a simulation of its growth using a 2D PIC code (FISCOF2). The SPW and the OTS phenomena have the essential role to explain the formation mechanism. When the laser beam irradiates boundary between the vacuum-plasma interface, the generation mechanism of SPW is considered.

Based on the collective behavior of the excited electrons in the y-direction due to the electric field component of the laser beam. The bidirectional collective behavior of the electrons in both positive and negative y-direction, leads to form SPW and leads its propagation near to the interface, thus produce the so-called standing wave. The ponderomotive force of the standing wave F_{SPW} plays a significant role in forming seeds or tips for the development of periodic nanograting structures. The OTS instability affects the formed tips and grows them up to form complete structure from the periodic nanograting.

The electron density profile successfully showed growth enhancement over time. At t = 500 fs, periodic nanograting structures form at the interface of the sparse–intermediate area, with an interspace size of 0.5 μm. The interspaces sizes were found to agree with the theoretical results.

Chapter 5 shows a summary of the results and conclusions of chapters 3, 4.

Chapter 2

Properties of Plasma Physics and Particle in Cell Code

2.1   History of plasma physics

The American scientist, Irving Langmuir, at the beginning of 20th century, proposed the term of plasma physics after he found a similarity between the electrons, ions, and neutrons in an ionized gas to the fluid medium [33]. Between the 1920's and the 1930's some researchers have begun to study plasma physics term individually for solving some particular problems such as (i) studying the effect of ionospheric plasma on long distance shortwave radio propagation and (ii) gaseous electron tubes used for rectification, switching and voltage regulation in the pre-semiconductor era of electronics [4].

In the 1940's Alfvén suggested the existence of electromagnetic-hydro magnetic waves inside a conducted liquid after placing it in a static magnetic field. Alfvén finds that every motion of the conducted liquid gave rise to the electromagnetic force which gave rise to the electric current. Due to the effected of the static magnetic field, these electric currents gave mechanical force which changes the state of motion of the conducting liquid. These mechanical force and the raised electromagnetic force is what called electromagnetic-hydro magnetic waves or what is recently known as Alfven wave. The Alfvén wave has been used to explain many phenomena in astrophysics plasma [34]. In the early 1950's large-scale plasma physics based on magnetic fusion, energy research started in a different country. This type of research was an offshoot of thermonuclear weapon research. The progress of the fusion research was plodding through most of the 1960's. At the end of that decade, the Russian tokamak began producing plasma with much better results than the previous results during the previous two decades [35]. International agreement was established in the early 21st century to construct the international thermonuclear experiment reactor (ITER) designed to produce 500 Megawatts of fusion output power. Besides, inertial confinement schemes were also developed in which high power laser bombard millimeter diameter pallets of thermonuclear fuel [36].

By the 1980's a significant effort has been exerted by the researchers in order to use plasma in many practical applications. Plasma has been used as a medium with its particular characteristics

to explain many of the physical phenomena in the recent decade such as the formation mechanism of the periodic nanograting structures that have been observed on the material surfaces after irradiating the medium with a laser beam [9]. Besides, plasma physics also helped in destructing of toxic and harmful materials, creating of new materials. The thermal plasma can be used to destroy the solid, liquid and gaseous thermal barriers, antiwear coatings, while cold plasmas can be used for surface modifications of materials, ranging from the simple topographical changes to the creation of surface chemistries and coatings [37].

2.2   Criteria for the plasma state

First and foremost, plasma considers as a quasi-neutral gas with collective behavior [4]. After heating gas to high enough temperature, the atoms collide with each other and release their electrons and the plasma forms after a certain ratio of ionization. See Fig. 2.1. There are three parameters characterize plasma as fundamental parameters:

1. Number of the charged particle with density (n) (measured in particles per cubic cm for both electrons and ions).

2. The temperature T_j of each species (j represents electron or ion, measured in eV, where 1eV= 11,605 K).

3. The steady state magnetic field **B** (measured in tesla).
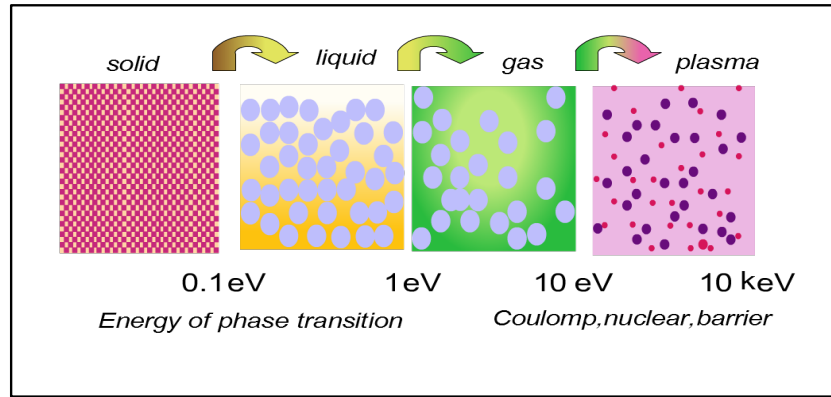
FIGURE 2.1: Schematic graph for the phase transition from the solid state to the plasma state with considering the required energy for the transition process [2].

Many plasma parameters can derive from the above three fundamental parameters (e.g., Deby length, Larmor radius, plasma frequency, cyclotron frequency, thermal velocity). The transition between a very weakly ionized gas and plasma occurs when the following conditions are satisfied:

1- The Debye length λ_D : is an essential parameter in plasma physics, and it is used as the scale over which electric fields are investigated out by a redistribution of the electrons is shown in the following

equation as follows:

$$\lambda_D = \sqrt{\frac{k_B T_e}{4\pi e^2 n_e}}, \tag{2.1}$$

the condition of any plasma system is that $\lambda_D \ll L$, where L is the system dimension.

Please consider that Eq. 2.1 is depends on $k_B T_e$ electron temperature which is measured in Kelvin, n_e electron density.

2- The number of charged particles inside the specific region must be more than one, i.e., $N_D \gg 1$, where

$$N_D = \frac{n\lambda_D^3}{3\varepsilon_o}. \tag{2.2}$$

3- The frequency of the plasma oscillations (ω) must be greater than the collision frequency with a neutral atom (ν)

$$\omega > \nu. \tag{2.3}$$

Fig. 2.2 shows plasma formation in relation to density and temperature. Plasma temperatures and densities ranging from cool and tenuous (like aurora) to very hot and dense (like the central core of a star).
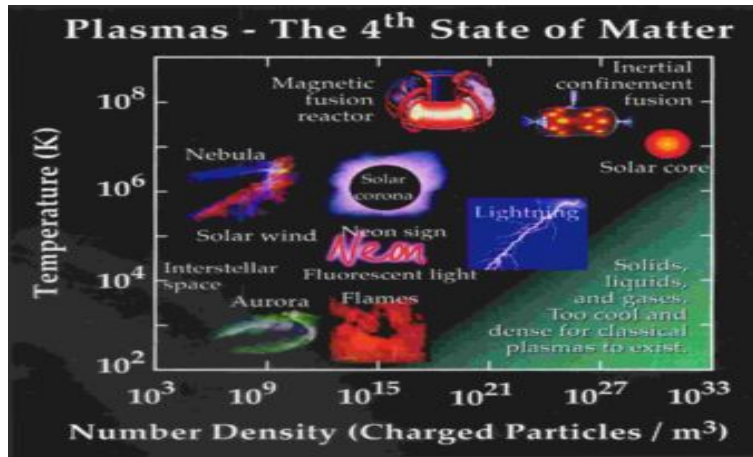
FIGURE 2.2: Shows naturally occurring and laboratory plasma in a relation between the plasma temperature and the density [3].

2.3 Theoretical description of the plasma physics

Plasma physics can define as the fourth case of matter, and it forms from an ionized medium-full with the separate charge (electrons and ions) in addition to the neutralized particles. For describing the plasma behavior due to the electric field and the magnetic field effects, one can use some models which depends on simple mathematical methods. We can summarize the most famous models that have been used to describe the plasma physics as follows:

2.3.1 Single particle model

2.3.2 Fluid model

2.3.3 Kinetic model and MHD model

2.3.1   Single particle model

In the single particle model, the motion of a single charged particle due to the effect of electric and magnetic fields has been studied. In this model, dealing with large numbers of charged particles can be quite tricky. Studying of the dynamic of the charged particles by using single-particle model will depend on analyzing the equation of motion for the charged particles in case of homogeneous and nonhomogeneous magnetic field. By calculating the value of the plasma particles velocities under the effect of the electric and magnetic field, we can understand the charge behavior. For example, the case of considering the equation of motion for a single particle under the effect of a static magnetic field with zero electric fields $\mathbf{E} = 0$ is shown as follows;

$$m\frac{d\mathbf{v}}{dt} = q(\frac{1}{c}\mathbf{v} \times \mathbf{B}), \tag{2.4}$$

where $\mathbf{v}$, q, and m are the velocity, charge, and mass of the charged particles while $\mathbf{B}$ is the static magnetic field. This reveals a circular orbit of a charged particle with the gyrofrequency or cyclotron frequency (ω_c) $\omega_c = qB_z/mc$ where the magnetic field $\mathbf{B} = B_z\mathbf{k}$ is along the z-axis in the Cartesian coordinate system and c is the light speed. We have observed that the angular gyrofrequency (ω_c) depends on the charge, mass and the magnetic field. In a case we studied the ions gyration, we found that the ions are gyrate from the clockwise while the electrons gyrate from the counterclockwise. See Fig. 2.3.
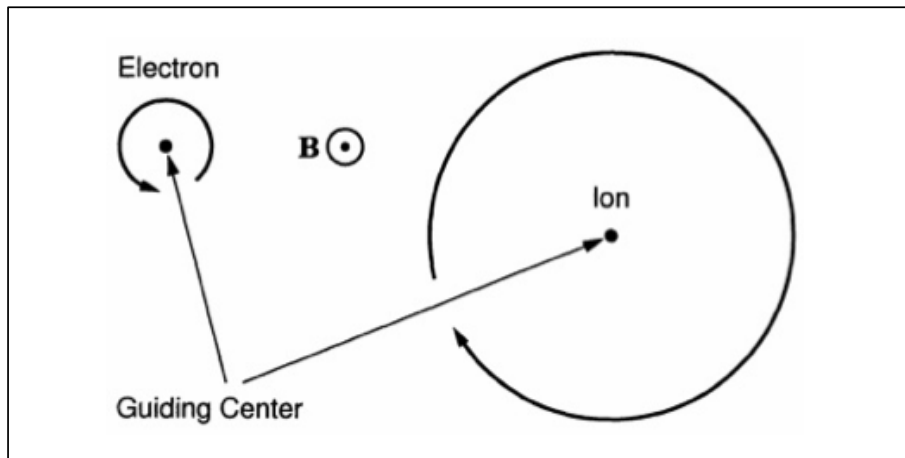
FIGURE 2.3: Shows the effect of the magnetic field motion on ions and electrons respectively [4].

Since the mass of the ions is 1836 times the electrons mass (e.g.Hydrogen), the ions would gyrate slower than the electrons. In this case, the particles would gyrate in a circular orbit across the external magnetic field with a constant velocity. The Larmor radius is given by $r_L = v_\perp/\omega_c$, where the velocity $v_\perp = \sqrt{v_x^2 + v_y^2}$ is perpendicular to the external magnetic field. We next consider a constant electric field $\mathbf{E}$, in addition to the magnetic field $\mathbf{B}$, we found that the gyrating motion is

combined with a drift of the guiding center, given by $\mathbf{v_E} = c(\mathbf{E} \times \mathbf{B})/\mathbf{B}^2$ which is perpendicular to both $\mathbf{E}$ and $\mathbf{B}$ fields, and is independently of the charge and mass of the plasma physics. This is called $\mathbf{E} \times \mathbf{B}$ drift. Note that the above result breaks down in the case where the magnetic field is so small that $\mathbf{E} \times \mathbf{B}$ drift becomes relativistic. In general, the charged particles response to the electric field and magnetic field in different drifts (e.g., the polarization drift, the curvature drift, the curvature drift, the Grad $\mathbf{B}$, etc. [4]).

2.3.2   Fluid model

In this model, the plasma physics treats as a fluid with neglecting the re-combination and ionization effects. By studying the continuity equation $(\partial n_j/\partial t) + (\nabla n_j \mathbf{v_j}) = \mathbf{0}$, where j indicate plasma species (electrons or ions) we can derive the zeroth velocity moment of the Vlasov equation and can calculate the non-relativistic momentum equation by multiplying the Vlasov equation with ($m\mathbf{v}$) as follows;

$$m_j n_j [\frac{\partial \mathbf{v_j}}{\partial t} + (\mathbf{v_j} \cdot \nabla)\mathbf{v_j}], = q_j n_j (\mathbf{E} + \frac{1}{c}\mathbf{v_j} \times \mathbf{B}) - \nabla \mathbf{P}_j \tag{2.5}$$

where $(\mathbf{E} + \frac{1}{c}\mathbf{v_j} \times \mathbf{B})$ is the electromagnetic force and $\mathbf{P_j} = \int m\mathbf{v}\mathbf{v}\mathbf{f_j}\mathbf{d^3V}$ is the pressure tensor, and we neglect the collisions between the plasma species. The common assumption is to replace the divergence of the pressure tensor with the gradient of the scalar pressure. Most scientists use the pressure equation from the ideal gas law $P = nk_BT$ and let temperature define by an adiabatic equation of state with T proportional to n^γ where γ is the ratio of specific heats. The Poisson equation can be used to close the relationship between the continuity equation and the momentum equation. The collisionless are valid when the electron-ion frequency is less than the plasma frequency. Such situations can happen in many physical phenomena: the earth magnetosphere, the pulsar magnetospheres, solar physics, and astrophysics [4].

2.3.3   Kinetic model and MHD model

Using of the single particle model is not always the effective model for describing the full plasma behaviour under the effect of the different parameters (e.g. electromagnetic fields, pressure, temperature, collision,..etc). It will be very simple and useful to understand the average description of the large number of plasma particles due to the collective behavior, using the kinetic theory with the single distribution function $f_j(\mathbf{r}, \mathbf{v}, t)$ we can define the dynamics of all identical particles inside plasma. The distribution function for the charged particles can be defined by the number of particles per cm^3 at position $\mathbf{r} = x\mathbf{i} + y\mathbf{j} + z\mathbf{k}$ and time t, with velocities $\mathbf{v} = v_x\mathbf{i} + v_y\mathbf{j} + v_z\mathbf{k}$ in a small volume dV of six-dimensional phase space. The plasma density can be described as: $n(\mathbf{r}, t) = \int f_j(\mathbf{r}, \mathbf{v}, t)d^3V$.

In order to consider the time evolution, the Vlasov equation can be used as follows;

$$\frac{\partial f_j}{\partial t} + \mathbf{v_j} \cdot \nabla f_j + \frac{q_j}{m}(\mathbf{E} + \frac{1}{c}\mathbf{v_j} \times \mathbf{B}) \cdot \nabla_{\mathbf{p}} f_j = 0, \tag{2.6}$$

where $q_j, \mathbf{v_j}, f_j$ the charges, perturbed velocities, and the normalized distribution function for different plasma species j. The electric field and the magnetic field inside the plasma can be calculated using the Maxwell equations as follows;

$$\nabla \times \mathbf{B} = \frac{1}{c}(4\pi\mathbf{J} + \frac{\partial \mathbf{E}}{\partial t}), \tag{2.7}$$

$$\nabla \times \mathbf{E} = -\frac{1}{c}\frac{\partial \mathbf{B}}{\partial t}, \tag{2.8}$$

$$\nabla \cdot \mathbf{E} = 4\pi e(n_i - n_e), \tag{2.9}$$

$$\nabla \cdot \mathbf{B} = 0. \tag{2.10}$$

Besides, for the non- relativistic kinetic theory, the charge and the current densities in plasma are also defined by:

$$\rho = \sum_j q_j n_j = \sum_j q_j \int f_j d^3V, \tag{2.11}$$

$$\mathbf{J} = \sum_j q_j n_j \mathbf{v_j} = \sum_j q_j \int f_j v d^3V. \tag{2.12}$$

Kinetic theory cannot be used for all cases especially when we want to deal with permeation charge fluids, the electron, and the ion fluid since the discrete particles must be neglected. Therefore, we used the fluid model to describe the plasma in such cases [4].

The magnetohydrodynamic (MHD) model can be used to describe a single charged particle fluid in which the electrons or ions are correlative and approximately have the same velocity. The MHD plasma model based on the electron gyro-frequency $\omega_c = eB_z/m_e c$ is much larger than $2\pi/T$, where T is the characteristic time-scale of the low–frequency phenomena. The MHD model can help in reducing the number of variables and removing the fast dynamical timescale. On the other hand, the fluid model can provide a system of calculation for the different charge fluid with different variables while MHD can be very helpful for the complicated nonlinear and inhomogeneous systems.

The mass density, mass flow velocity, the current density and the total pressure for a single particle fluid can be introduced as:

$$\rho = \sum_j m_j n_j = m_e n_e + m_i n_i = n(m_e + m_i) \approx nm_i, \tag{2.13}$$

$$\mathbf{v} = [m_e n_e \mathbf{v_e} + m_i n_i \mathbf{v_i}]/\rho = [m_e \mathbf{v_e} + m_i \mathbf{v_i}]/[m_e + m_i] \approx \mathbf{v_i}, \tag{2.14}$$

$$\mathbf{J} = \sum_{\mathbf{j}} q_i n_j \mathbf{v_j} \approx en(\mathbf{v_i} - \mathbf{v_e}), \tag{2.15}$$

$$P = P_e + P_i \approx nk_B(T_e + T_i), \tag{2.16}$$

for the low frequency phenomena in plasma and when the ion plasma frequency is larger than the gyrofrequency and when the temperature is constant we can find that $n_e = n_i = n$ [4].

2.4   Waves in plasma physics

Plasma considers as the fourth state of matter which consists of separate charged particles with high electric conductivity. Plasma physics strongly respond to the electromagnetic fields. Both electrostatic and electromagnetic waves of different frequencies can propagate inside the plasma. For describing the linear wave phenomena in a homogeneous plasma, calculating the dispersion relation is mandatory since the frequency ω is associated with the wavenumber k. The phase velocity and the group velocity can be defined in term of k and ω as follows;

$$V_{ph} = \frac{\omega}{k} = \frac{dx}{dt}, \tag{2.17}$$

$$V_g = \frac{\partial \omega}{\partial k}, \tag{2.18}$$

the phase velocity can help in determining the speed and the direction of the wavefront or phase since the phase velocity is directed parallel to $\mathbf{k}$. The group velocity can help in determining the direction of the energy flow and also provide us with information contained in the wave [4].

2.5   Electrostatic waves in unmagnetized plasma

The space charge waves are the compression and rarefaction waves of the charged particles. The phase velocity of the electrostatic waves ranges from the electron thermal speed v_{te} to infinity. Some particles in the plasma can be in resonance with the space charge waves when the Doppler shifted frequency equal $\omega - k \cdot \mathbf{v} = 0$. In that case, the charged particles can be efficiently accelerated/ decelerated by the wave.
Consider an electrostatic wave with form;

$$\mathbf{E} = A sin(\omega t - kx) \, \mathbf{i},$$

the electrostatic wave which moves with the phase velocity will have the shape of:

$$\mathbf{E} = A sin(k \cdot \Delta \cdot t) \, \mathbf{i},$$

the electron velocity in the x- direction will be known as for resonant electrons;

$$\Delta = v_x - \omega/k.$$

When Δ is less than the phase velocity $\Delta \ll \omega/k$, we can divide the resonant electrons into two groups:

(A) $\Delta > 0$ and (B) $\Delta < 0$,the electrons that have same group velocity and uniform distribution along x- axis can be accelerated since $v_x > \omega/k$.

To move faster into the decelerating zones and retarding in the decelerating zones to spend more time, there is a bunch of group A electrons transferring energy to the wave. The slower moving electrons $v_x < \omega/k$ tend to bunch in the accelerating zones, gaining energy from the wave.The slope of the velocity distribution function at $v_x = \omega/k$.

whether the wave is going to grow or damp. Using the kinetic theory, in this case, is very useful to study the response of the plasma particles to the electrostatic field [4]. There are two waves related to the electrostatic wave: Langmuir wave and the ion acoustic wave. For studying this waves, we will depend on solving the Vlasov equation for the response of the electrons in the presence of a Langmuir wave in a collisionless plasma. Vlasov equation can be used to study the response of the ions in the ion acoustic wave.

2.6   Particle in Cell code

Particle in cell (PIC) code is a technique placed for solving some groups of partial differential equations by tracking of charged particles in constant electromagnetic (or electrostatic) fields. Also, PIC code tracing the charged particle on a fixed mesh in a Eulerian frame in continuous phase space [38]. The densities and currents of the charged particles are computed simultaneously on Eulerian (stationary) mesh points. PIC code gained a lot of scientists attraction especially for plasma physics simulation since late of the 1950s and early of 1960s by Buneman, Dawson, Hockney, Birdsall, Morse, and others. Even before the first FORTRAN compilers were available, PIC methods were already in use [39]. The general idea for using the PIC code depends on the study the plasma behavior for the real case with decreasing of a number of charged particle inside simulation systems. Number of charged particles can be calculated by using the following equation;

$$N_D = n\lambda_D^3. \tag{2.19}$$

The intention to study the collective behavior of the collisionless plasma in any systems is due to it is longer than Debye length. We can alter the simulation by using smaller N_D in PIC code so that we can keep the essential plasma behavior. PIC code can measure the motion of charged particles within two steps:

Firstly, we will calculate the electromagnetic field by using Maxwell's equations by using the initial currents and charge densities. Secondly, we use the calculated electromagnetic fields from the previous step within Newton equation to move the charged particles for a short distance. Therefore, we are going to recalculate the electromagnetic fields from new particle positions and charge density. Repeating the above steps within the simulation time and simulate particle movement in the mean field surrounding them help in getting the output results. The physical volume of the simulation system was divided into cells by using parallel lines to the boundary for the seek of decreasing and avoiding errors. This can be done by calculating the equation of motions and Maxwell's fields in a continuous space and time. At the intersections of these lines, we present a set of points which will be defined as mesh points or grid points. The calculation of the charge fields is placed within these mesh points, and relative to these points we move the particles [40, 41]. The charged particles with their spatial coordinates are continuous and can occupy position anywhere within the mesh. Simulation work as we mentioned above is done in two major steps and some internal sub-steps. First step based on reading the initial conditions, particle positions and velocities. In second step weighting has to be done for charged particles because the calculation of charge density in the mesh grid point depends on the distance of the particle from that point. After getting charge densities, we conduct with the integration of field equations, and then we weight how the field in individual mesh grid point impact each particle. The last step is integrating the equation of motion, charge position, and velocity of particles. Then we repeat the procedure until we obtain the wanted result. The computation cycle can be seen in Fig. 2.4.
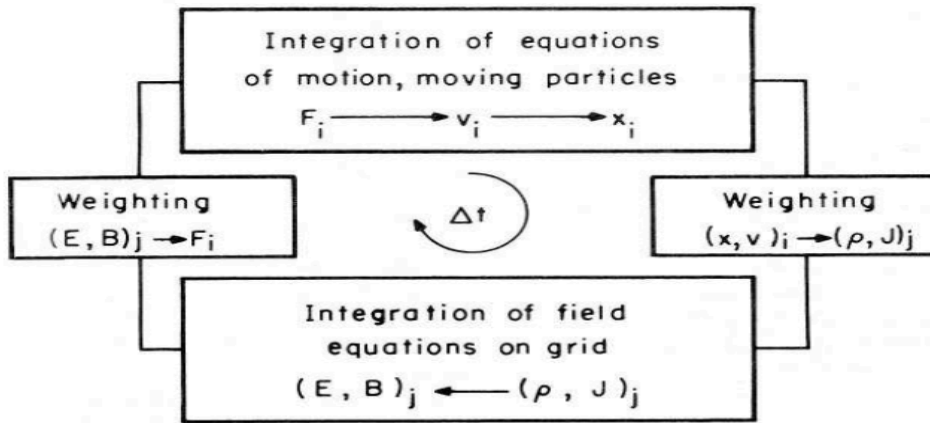
FIGURE 2.4: Computation cycle source [5].

The calculation of the PIC code depends mainly on using both Maxwell equation from Eq. 2.7 and the relativistic equations of motion for providing the required details of the fields $\mathbf{E}$, $\mathbf{B}$ and the current density $\mathbf{J}$ for each charged particle as follows;

$$m\frac{d\mathbf{u}}{dt} = q(\mathbf{E} + \frac{1}{\mathbf{c}}\mathbf{v} \times \mathbf{B}), \tag{2.20}$$

$$\frac{d\mathbf{x}}{dt} = \mathbf{v} = \frac{\mathbf{u}}{\gamma}, \tag{2.21}$$

$$\gamma = \frac{1}{\sqrt{1-(\frac{\mathbf{v}}{c})^2}} = \sqrt{1+(\frac{\mathbf{u}}{c})^2}, \tag{2.22}$$

where $\mathbf{E}$, $\mathbf{B}$ are the electric field and Magnetic Field, respectively. and $\mathbf{u}, \gamma$ are the velocity vector and the relativistic factor, respectively.

2.7   Conclusion

The plasma physics considers as the fourth state of matter. Several models have been assumed to study plasma physics from a different point of views such as; Single particle model, Fluid model, Kinetic model, and MHD model. Those model helped to explain and analysis many of physical phenomena. Particle in Cell code has been used to study plasma physics in simulation system and has contributed to give details of the internal interaction of the plasma system by tracing its particle velocities, fields, and current densities.

Chapter 3

Formation Mechanism of Periodic Nanograting Structure by Weibel Instability

3.1 Introduction

Since 1999, self-organized periodic nanograting structures have been reported after irradiating the solid material surfaces with an ultrafast laser beam. Many researchers introduced the periodic nanograting structures on surfaces of some material such as insulators [12, 15, 16], semiconductors [17], and metals [18, 19] as a way for advanced applications. Researchers show the orientation of the periodic structure is perpendicular and/or parallel to the polarization direction of the laser beam [11, 20]. The repeated irradiation of ultrafast laser on the material surfaces has a great advantage in creating periodic nanograting structures and for upgrading the material properties. Advanced material properties have been designed on a macroscopic scale. Nowadays, several applications come up with the help of periodic nanograting structures in different fields e.g of functional bio-materials [21, 22], tribology for friction reduction [23], Chemistry for protein folding [25], and engineering for metal coloring [26].

In this chapter we are going to introduce how the periodic nanograting structures can be formed by using relativistic laser beam of the parameters of $I = 10^{18}$ W$/cm^2 - \mu m^2$, $\lambda_L = 800$ nm, rise time $\tau = 15 fs$, and plane wave. Laser beam irradiated continuously onto the target at a normal incidence angle. We have used hydrogen plasma as the target plasma to study the formation mechanism in order to decrease the calculation time in the simulation systems. We have used FISCOF2 (PIC code) to investigate and analyze our formation mechanism, FISCOF2 is able to deal with different type of materials that have higher atomic number and mass number than hydrogen for the reality calculations. The Weibel instability shows major role to explain our formation mechanism for the case of the relativistic laser beam.

16

Sections 3.2 and 3.3 show the simulation system and the simulation results. Section 3.4 shows general idea about the Weibel instability and the role of the Weibel instability in the explaining the formation mechanism. Section 3.5 is a conclusion of this chapter.

3.2   Simulation framework

We have studied the dynamics of laser-plasma interaction in our simulation framework by using FISCOF2. In the mimic-target plasma interface, the framework is formed from two regions which are surrounded by vacuum everywhere. The first region defined as mimic plasma with assumed electron density of value n_{mimic} of 0.7 n_{cr}, where n_{cr} is the critical density. The mimic plasma resizes along x-axis from 0 to 2 μm and along the y-axis from -3.6 to 3.6 μm as shown in Fig. 3.1. The second area defined as (dense) target plasma with the assumed electron density of value n_{target} of 10 n_{cr}. The target plasma resides on the x-axis in the range 2 to 12 μm and on the y-axis in the range – 3.6 to 3.6 μm. The mimic plasma's thickness is about 2 μm along the x-direction of the (x, y) plane, while the target plasma is about 10 μm along the x-direction of the (x, y) plane. The laser beam injected onto the surface from the left side in a plane wave as indicated by the black arrow.
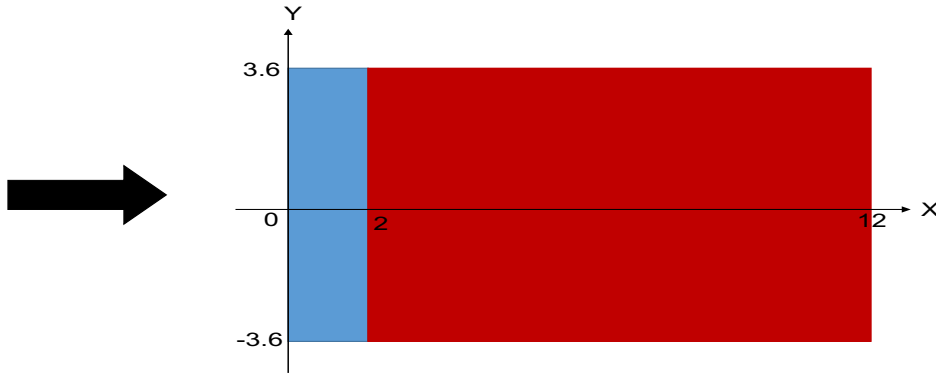
FIGURE 3.1: A schematic drawing of the simulation framework. The schematic shows the target plasma with dimension $x = 2 \sim 12$ μm, $y = -3.6 \sim 3.6$ μm and density $n_{target} = 10$ n_{cr} and mimic plasma with dimension $x = 0 \sim 2$ μm, $y = -3.6 \sim 3.6$ μm and density $n_{mimic} = 0.7$ n_{cr}. The vacuum area surround the simulation framework from all sides. The laser beam is being irradiated continuously for about 500 fs from the left hand side of the system.

The laser beam intensity of $I = 10^{18}$ W/$cm^2 - \mu m^2$, laser wavelength of $\lambda_L = 800$ nm, and laser rise time of $\tau = 15$ fs is irradiated continuously onto the target plasma at normal incidence. In our simulation, the laser parameters are used together with the hydrogen plasma to produce periodic nanograting structure. The plasma characterizes by electron temperature $T_e = 1$ keV, ion temperature $T_i = 0.1$ keV, and the ion electron mass ratio $M_i/m_e = 1836$. The periodic nanograting structure has been clearly self-organized at the boundary between mimic plasma and target plasma at t = 250 fs, as shown in Fig. 3.2. At t = 250 fs, 13 tips from the periodic nanograting structure are formed along y-axis from -3.0 to 3.0 μm, and the average interspace size of 0.46 μm is shorter than the laser wavelength of 0.8 μm.
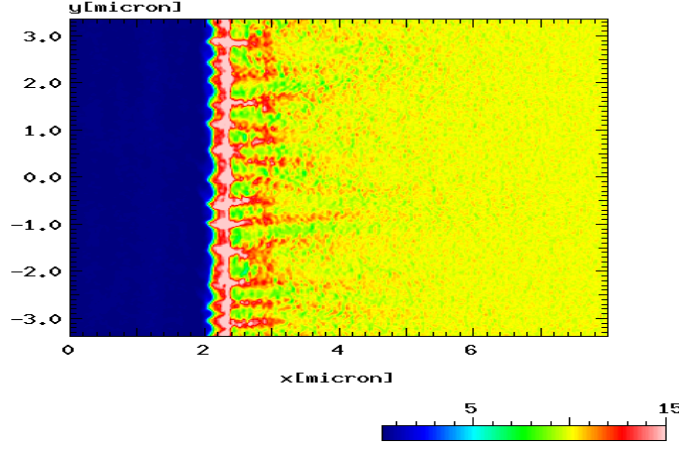
FIGURE 3.2: Electron density profile in the x-y plane at snapshot t = 250 fs. The electron density profile shows the effect of the time evolution on the periodic nanograting structure. The periodic nanograting structure observed as self-organized structure along the boundary between mimic plasma and target plasma at t = 250 fs. 13 tips from the periodic nanograting structure are formed along y-axis from -3.0 to 3.0 μm, and the average interspace size of 0.6 μm is shorter than the laser wavelength of 0.8 μm.

3.3   Simulation results

Figs. 3.3, 3.4 and 3.5 show the magnetic field profile in the z-direction (B_z), the electron current density profile in the x-direction (J_{xe}), and the electron density profile in snapshots, respectively at time (a) t = 150 fs and (b) t = 200 fs. By referring to the negative value of the x-direction component of the current density J_{xe} around the point y = 0 μm in Fig. 3.4 (b), we didn't observe any periodic nanograting structure in the electron density profile by referring to the same point y = 0 μm in Fig. 3.5(b). The negative value and the positive value of the z- direction component of the magnetic field B_z is found above and below y= 0 μm in Fig. 3.3.

Around the point y = 0.3 μm we can observe the periodic nanograting structure in Fig. 3.5 (b). in Fig 3.4 (b), the positive x-component of the electron current density J_{xe} around point y = 0.3 μm is consistent with the enhanced magnetic field B_z in Fig. 3.3 (b). The positive z-component of the magnetic field B_z observed in Fig. 3.3 (b) is shown above of the point y = 0.3 μm approximately at y= 0.5 μm while the negative component of B_z is shown below of the point y = 0.3 μm approximately at y= 0.1 μm. The positive component of the electron current density J_{xe} in Fig. 3.4 (b) is consistent with increasing of the electron density and forming of the tips at the boundary between the mimic and the target plasma in Fig. 3.5 (b). These tips are essential for forming the periodic nanograting structures. We can observe the same phenomena in Fig. 3.5 (b) at the locations y = - 0.8, - 0.6, -0.2, 0.3, 0.9 μm. These locations are clear evidence to prove the formation of the periodic nanograting structure by the Weibel instability.
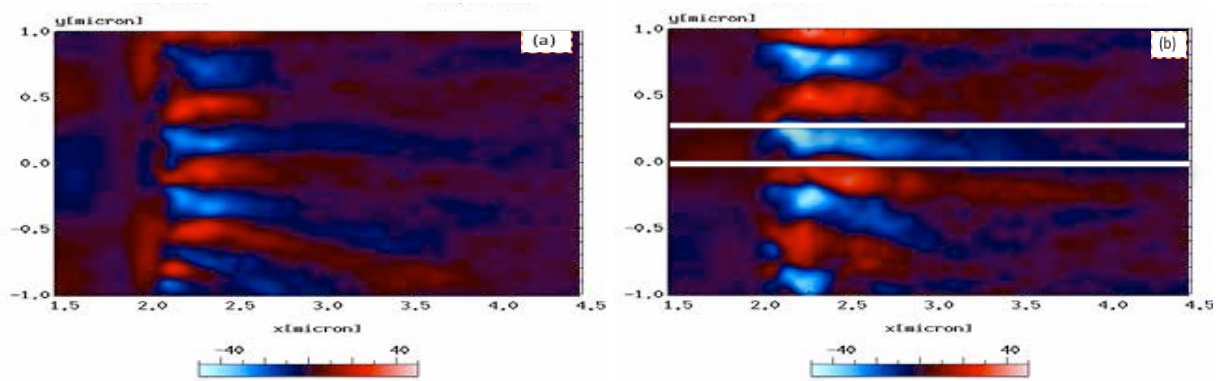
FIGURE 3.3: Simulation results for the magnetic field B_z in the x-y plane at snapshots (a) t = 150 fs, (b) t = 200 fs. The simulation results show the growth of the magnetic field B_z with time evolution. The white lines around y = 0 μm and around y = 0.3 μm which is shown in (b) are used to explain the growth of the magnetic field B_z according to the growth of the current field J_{xe}. The observed growth of B_z between snapshots (a) and (b) explains the reason of forming the Weibel instability. The enhanced B_z between snapshots (a) and (b) are considered as the reason of forming periodic nanograting structure.
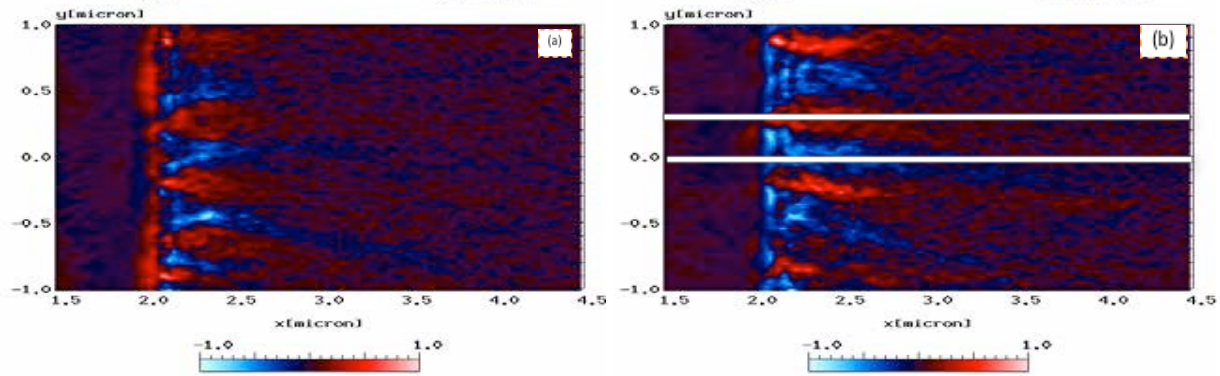
FIGURE 3.4: Simulation results for the electron current density J_{xe} in the x-y plane at snapshots (a) t = 150 fs, (b) t = 200 fs. The electron current density J_{xe} simulation results show the growth of electron current density J_{xe} with time evolution and this is reason of creating the periodic nanograting structure. The white lines around y = 0 μm and y = 0.3 μm which are shown in (b) are used to explain the growth of the electron current density J_{xe} with time evolution. Around y = 0 μm the negative component of J_{xe} can be observed while the positive component of the electron current density J_{xe} is seen around y = 0.3 μm. At the locations y = - 0.8, - 0.6, -0.2, 0.3, 0.9 μm, the positive component of J_{xe} have been recorded. These values of the positive J_{xe} are reasons of increasing the growth of B_z which will followed by the growth of the periodic nanograting structure as will observe in the electron density profile.
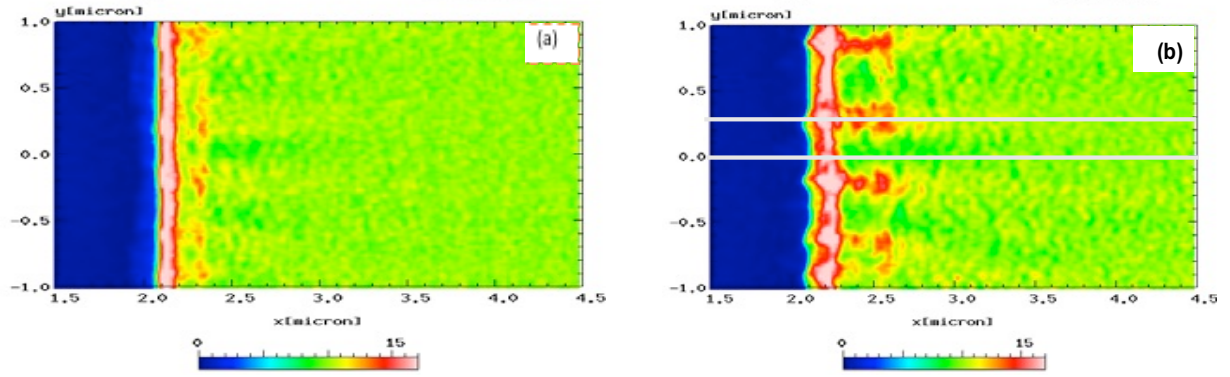
FIGURE 3.5: Electron density profile in x-y plane at snapshots (a) t = 150 fs, (b) t= 200 fs. The white lines around y = 0 and 0.3 μm are used to show the growth of periodic nanograting structure with time evolution. We cannot observe periodic nanograting structure around y = 0 μm while it can be observe clearly around y = 0.3 μm. The positive component of the electron current density J_{xe} is consistent with forming the periodic nanograting structure. Moreover, the enhanced magnetic field B_z has a major role in increasing the concentration of the electrons in some points which will form later the periodic nanograting structure.

3.4   Weibel instability

Weibel instability is one type of a plasma instability that can be observed and recorded after the interaction of the high intensity laser (relativistic intensity) with the homogeneous and inhomogeneous plasma due to anisotropy in velocity and temperature difference between different species inside the plasma. In 1959, Weibel [42] has succeeded for the first time to calculate the transverse waves which spontaneously grown in a plasma with anisotropic velocity distribution. The mechanism of instability is mainly shown in the curvature of the electrons due to magnetic field that causes a momentum flux which in turn effects $< \mathbf{v} >$ (and hence $< \mathbf{J} >$) in such a way as to increase the fluctuation field [43].

Weibel instability has a broad range of applications in astrophysical plasma, as shown in [44], as well as in laboratory plasma [45, 46]. Also, Weibel instability can explain the generation of a magnetic field in the vicinity of gamma-ray burst sources, supernovae and galactic cosmic rays [47, 48]. In the simple case of unmagnetized plasma, Weibel instability has been extensively studied in both relativistic and nonrelativistic regimes [49, 50]. Within this thesis, Weibel instability has been used to explain the formation mechanism of the periodic nanograting structure by using relativistic laser intensity ($I = 10^{18}$ W/$cm^2 - \mu m^2$) [9].

Within our simulation case, The enhancement of magnetic field due to the Weibel instability inside plasma is used to explain the formation mechanism of the periodic nanograting structures. We have assumed low density mimic plasma in front of the target plasma instead of initially preformed plasma in the experimental area. Under the effect of the laser beam on plasma, two counter streams of the electron have been formed. The red arrows represent the fast electron streams which are produced due to ($\mathbf{J} \times \mathbf{B}$) heating mechanism by the laser [51] , as shown in Fig. 3.6 (a). Assume that there is an electron at rest on the mimic plasma.

After irradiation, the electron is accelerated in a direction perpendicular to the laser beam propagation direction. Under the effect of the Lorentz force ($\mathbf{v} \times \mathbf{B}$), the electron is bent and is injected into the target plasma. Due to laser reflection, the electrons moves freely to the right-hand side of the target plasma without any laser beam effect. Fig. 3.6 (b) shows the formation of the blue arrows which is called the return electron streams. The return electron streams are produced due to the current neutrality. Due to the current neutrality, the return electron streams will be dragged in a direction opposite to the fast electrons. The return electron streams are much thicker than the fast electrons because the number of the returned electrons is much larger than the number of the fast electrons. In Fig. 3.6 (c), we assume the existence of the perturbed magnetic field with periodicity. In Fig. 3.6 (d), the magnetic field causes the curvature of the fast and return electrons. The degree and the direction of bending can be easily analyzed by using Lorentz force. For the return electron streams arrows, they have bent more than the fast electron arrows due to their low velocity. This bending produces net electron density currents which will be represented as black arrows. The black arrows enhance the initial magnetic field as seen in Fig. 3.6 (e). Once the return electron concentration increase near to the plasma boundary, the tips form and spread at regular interspace in Fig. 3.6 (f). These tips
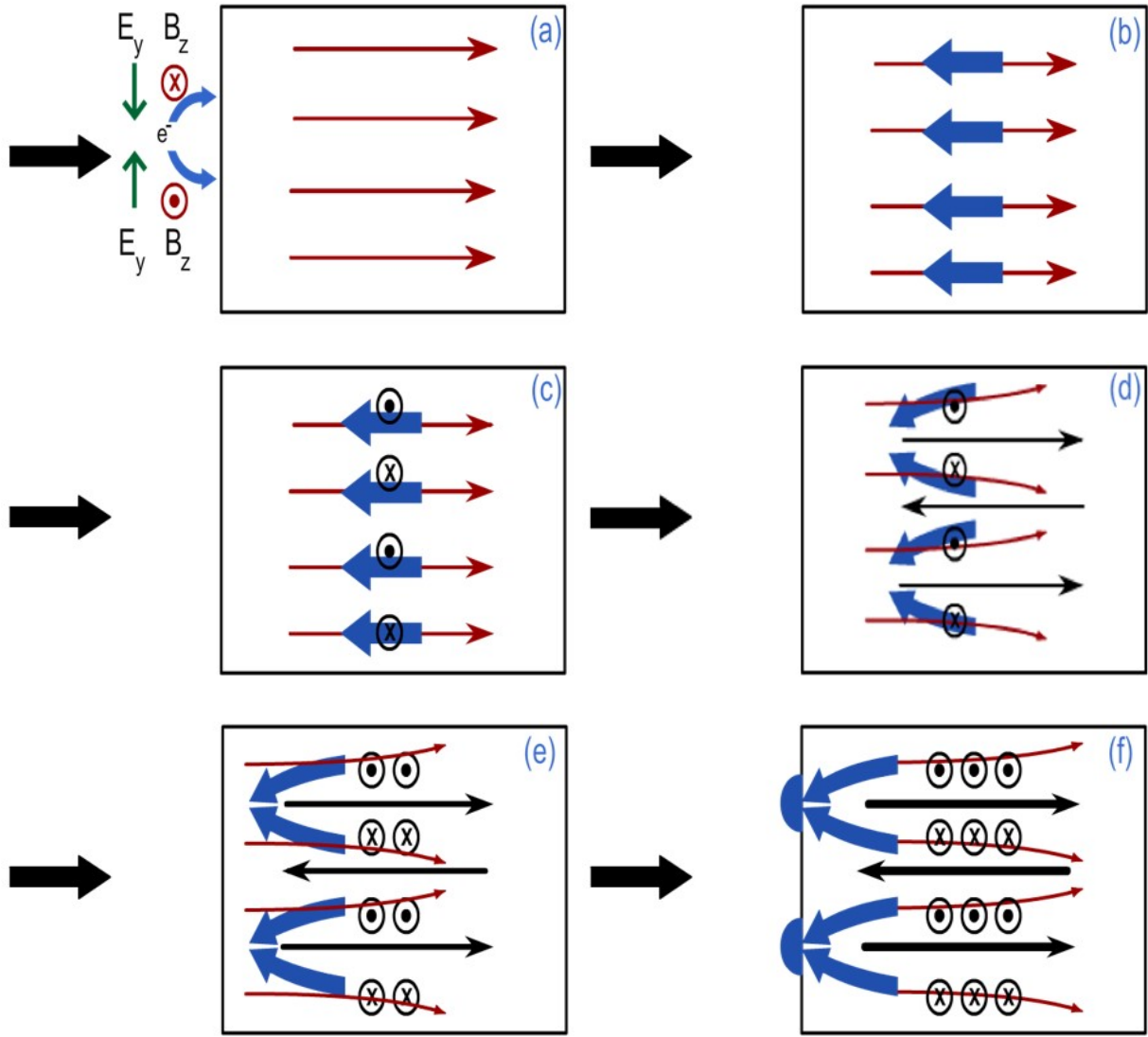
FIGURE 3.6: A schematic drawing of the Weibel instability role in forming of the periodic nanograting structure in the target plasma. The formation mechanism process has been graphically drawn step by step beginning from laser irradiated the surface of the mimic-target plasma interface at Fig. 3.6 (a) and ending with the formation of the periodic nanograting structure at Fig. 3.6 (f). Weibel instability phenomenon has been recorded in Fig. 3.6 (e) as a result of the enhancement of the magnetic field with time evolution due to the net electron current density (the black arrows) in Fig. 3.6 (d).

lead to form of the periodic nanograting structure. The growth of the magnetic field and in the net current density is what well-known as the Weibel instability.

Figs. 3.7 and 3.8 shows the effect of the time evolution on both of the electron current density J_{xe} and the magnetic field B_z, respectively. The growth of the magnetic field B_z and the electron current density J_{xe} are clearly shown with time evolution. Thus, the growth is presented substantial evidence of occurring the Weibel instability and then the formation of the periodic nanograting structure is followed.
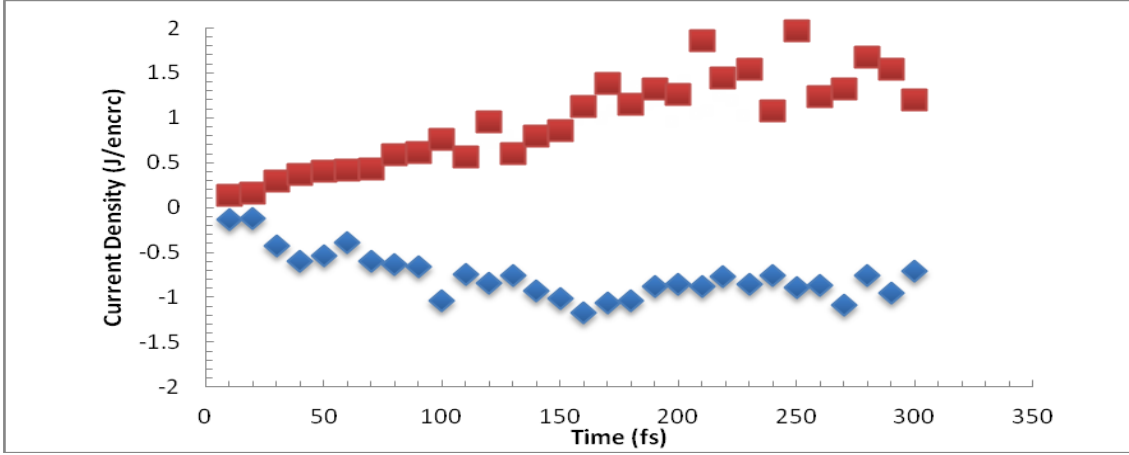
FIGURE 3.7: Plotting for time enhancement of the electron current density J_{xe} . The electron current density J_{xe} with blue diamonds and red squares indicate maximum and minimum values, respectively. This growth of the J_{xe} with time evolution is the reason of growth of the Weibel instability and forming of the periodic nanograting structure.
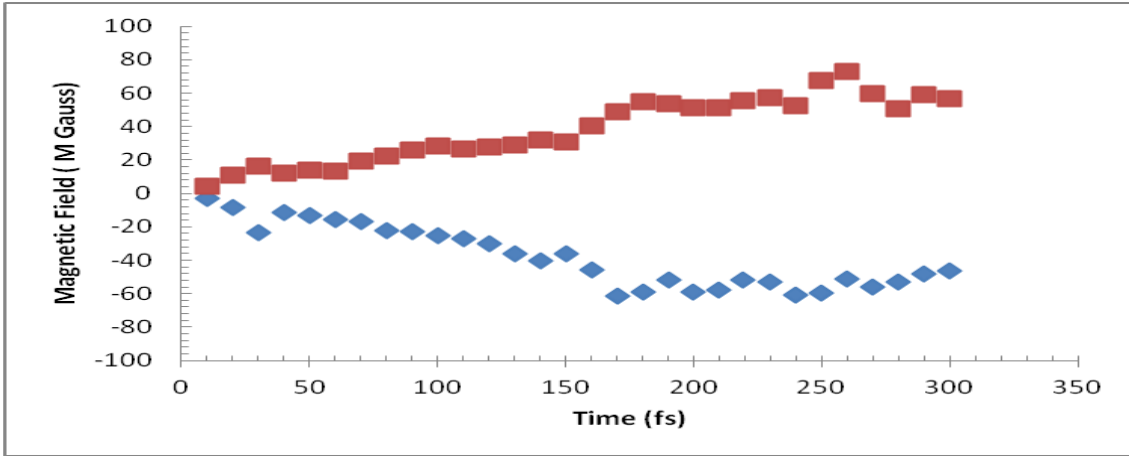
FIGURE 3.8: Plotting for time enhancement of the magnetic field B_z .The magnetic field B_z with blue diamonds and red squares indicate maximum and minimum values, respectively. The growth of B_z over time is what well known as Weibel instability.

3.5   Conclusion

This chapter explains the formation mechanism of the periodic nanograting structure by using a relativistic laser beam. The Weibel instability has been introduced in this chapter as the related physics to clarify the reasons of this phenomenon. The laser beam of intensity 10^{18} W/$cm^2 - \mu m^2$, and the wavelength of 800 nm, and rise time $\tau = 15$ fs used to excite the periodic nanograting structure along the interface between the mimic-target plasma. The enhanced magnetic field, together with the electron current density and the electron density, has been calculated by the particle in cell code (FISCOF2) with time evolution. The periodic nanograting structures at t = 250 fs is formed 13 tips along y-axis from -3.0 to 3.0 μm, the interspace size of 0.46 μm is shorter than the laser wavelength. The periodic nanograting structures observed at y = -0.8, -0.6, -0.2, 0.3, and 0.9 μm in the electron density profile where the positive x-component of the electron current density J_{xe} exist. Furthermore,

the positive and the negative z-component values of the enhanced magnetic field B_z are shown in between above positions. For example at y = 0.3 μm, the positive z-component of B_z exists at y = 0.5 μm while the negative z-component of B_z exists at y = 0.1 μm. The above description shows the consistence between the enhanced magnetic field and the electron current density which leads to producing periodic nanograting structure and confirm the existence of Weibel instability and its role in the formation mechanism.

Chapter 4

Formation Mechanism of Periodic Nanograting Structures by Surface Plasma Waves

4.1   Introduction

The mechanism of periodic nanograting structures can be considered as a contemporary topic in science. Many researchers have attempted to explain the formation mechanism of periodic nanograting structure by assuming different growth model [10, 52–56]. In this chapter, we explain how periodic nanograting structure are formed in the case of irradiating plasma with nonrelativistic laser beam using a vacuum-plasma interface simulation framework. Plasma physics and its related phenomena are evoked to explain the mechanisms behind this pattern formation, including the Surface Plasma Wave (SPW) and the effect of the Oscillating Two Stream Instability (OTS) in the target plasma. The ripples on the metallic surfaces have been observed in many experiments after multi-pulses femtosecond laser beam [7]. Our simulation results reveal that an irradiation period of the laser beam of 500 fs is required to obtain the periodic structure.

In sections 4.2 and 4.3 the simulation framework and results are provided, respectively. An elaborate description on how the periodic nanograting structure begins and how is SPW used to explain the phenomena is provided in section 4.4. In section 4.5 OTS has been used to complete the explanation of the formation mechanism. Finally, Section 4.6 provides a brief conclusion.

4.2   Simulation framework

In the vacuum-target plasma interface, the framework of the present simulation system is formed by one limited region which is surrounded by vacuum everywhere. This area contains (dense) target plasma with the assumed electron density of value n_{target} of 10 n_{cr}, where n_{cr} is the critical density.

25

The target plasma resides on the x-axis in the range 2 to 12 μm and on the y-axis in the range – 10 to 10 μm. We consider a nonrelativistic laser beam with flat-top profile shape being continuously irradiated onto the target at normal incidence for about 500 fs See Fig. 4.1. The laser beam parameters are defined in our simulation framework as follows ; intensity of $I = 10^{16}$ W/$cm^2 - \mu m^2$, wavelength of λ_L = 800 nm, full wave half maximum of $\phi_{FWHM} = 10 \ \mu m$, and rise time $\tau = 5$ fs. In the 2D simulation framework, we chose a p-polarized laser beam to form the periodic nanograting structure. Since there is no periodic nanograting structure has been observed when we choose an s-polarized laser beam.
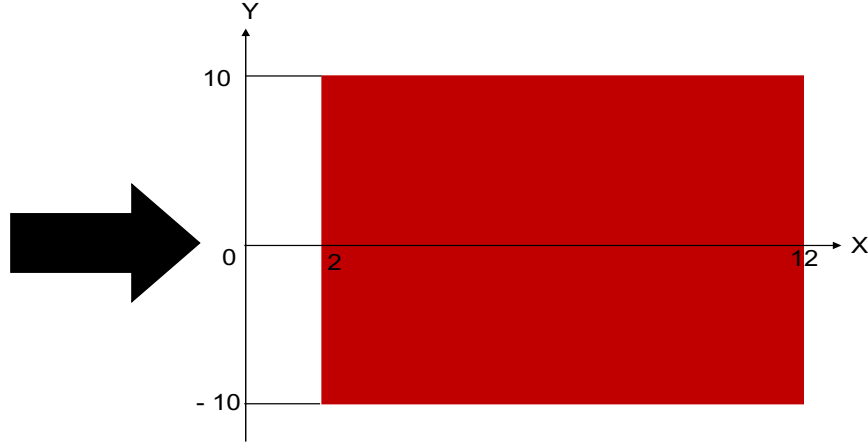
FIGURE 4.1: A schematic drawing of the simulation framework. The schematic shows one region called target plasma and placed in the x-and y-dimension $x = 2 \sim 12 \ \mu m$, $y = -10 \sim 10 \ \mu m$. The target plasma density is $n_{target} = 10 \ n_{cr}$. The vacuum area are surrounding the target plasma from everywhere. The laser beam of intensity $I = 10^{16}$ W/$cm^2 - \mu m^2$ irradiated from the left hand side of our simulation framework.

Using the present framework for simulation, the hydrogen plasma properties are defined based on an electron temperature T_e of 1 keV, ion temperature T_i of 0.1 keV, and a mass ratio M_i/m_e of 1836/16, where M_i and m_e are the ion and the electron mass, respectively. The chosen mass ratio value aims to reduce the time required for calculation. The formation mechanism was studied using the 2D Particle In Cell code FISCOF2 [41].

4.3   Simulation results

The simulation results for the periodic nanograting structure have been generated by FISCOF2. The electron density profile shows the formation of the periodic nanograting structures with time evolution Fig. 4.2. Snapshots at different times shown in Figs. 4.2 (a)- 4.2 (h) can provide details on the sequential formation mechanism of periodic nanograting structures. At t=150 fs in Fig. 4.2(a), we observe that a small intermediate area of density n_{inter} is formed. This intermediate area can be formed naturally due to plasma expansion [57] and its size grows with the time evolution accordingly.

In the Fig. 4.2 (a) t= 150 fs, (b) t= 200 fs, (c) t=250 fs, (d) = 300 fs, (e) t= 350 fs, (f) t= 400 fs, (g) t= 450 fs, and (h) t= 500 fs show a series of the snapshots used to illustrate formation of the periodic

nanograting structure with time evolution. With plasma expansion and time evolution, the vacuum in front of the target plasma region no longer exists since there are small density values surrounding the target plasma begin to be recorded (hereinafter referred to as sparse density n_{sparse}).
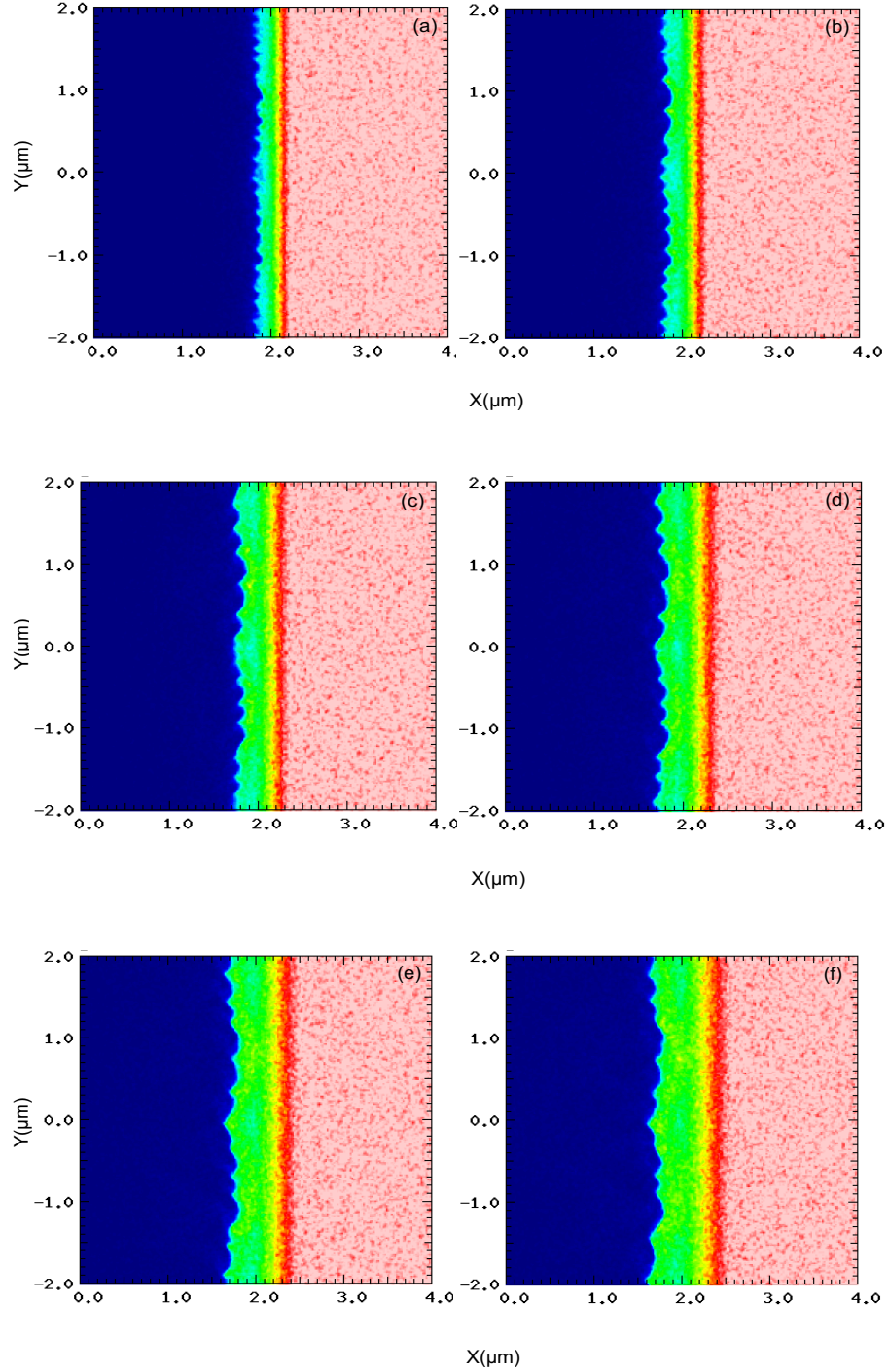
To explain how the periodic nanograting structure can be formed after irradiating the vacuum-plasma interface with laser beam of intensity $I = 10^{16}$ W/$cm^2 - \mu m^2$, and wavelength of $\lambda_L = 800$ nm for about 500 fs, SPW and OTS will be used to explain the formation mechanism of the periodic nanograting structures in our simulation framework. With the help of FISCOF2, we were able to check the details of nanograting structures over time. Beginning with t = 150 fs, we observed a
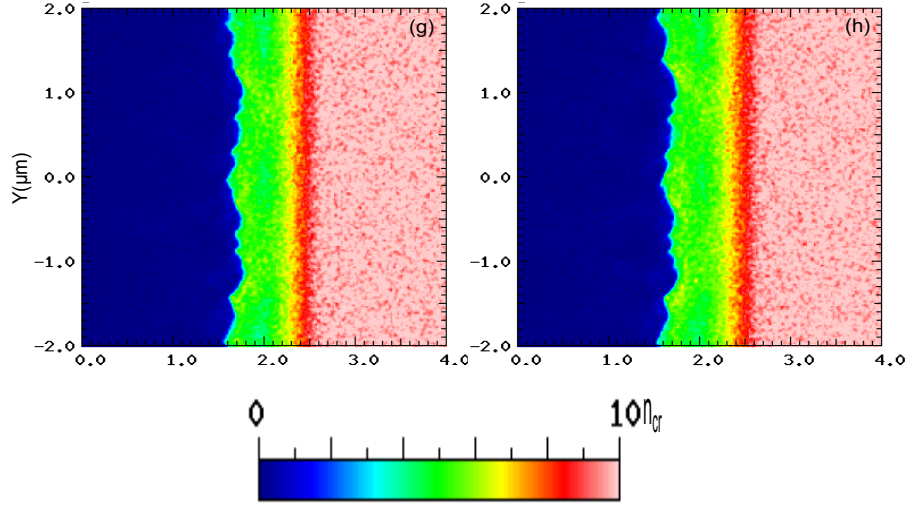
FIGURE 4.2: The electron density profile in the x-y plane in snapshots taken at (a) t =150 fs, (b) t =200 fs, (c) t = 250 fs, (d) t = 300 fs,(e) t = 350 fs,(f) t = 400 fs, (g) t = 450 fs, and (h) t = 500 fs. Fig. 4.2 shows a series of the snapshots used to illustrate formation of the periodic nanograting structure with time evolution. With plasma expansion and time evolution, the vacuum in front of the target plasma region no longer exists since there are small density values surrounding the target plasma begins to be recorded. The size of the periodic nanograting structures change with time evolution. At the early time tips or seeds of the periodic nanograting is clearly seen, with time evolution we can observe a full periodic nanograting structure.

clear periodic structure, but the structure was of a small size. With time evolution, the structure began to grow up, and self-organize along the interface between two new regions: sparse region and intermediate area. To show the effect of the time evolution on the growth rate of periodic nanograting structures, we need to measure the electron densities in both sparse and intermediate areas. A high degree of accuracy should be considered through the calculation of the electron densities n_{sparse} and n_{inter} values.

The average electron densities (n_e/n_{cr}) were estimated using FISCOF2 and are shown in the Fig. 4.3, as relational graphs with x-axis. The average electron densities show increasing concentration in the intermediate area as time evolves. The average electron density at times t = 200, 300, 450, and 500 fs are shown by the blue, purple, green, and orange curves, respectively. In Fig. 4.4 the same data is shown within the limited region between x = 1 and 2 μm, where the initial transition from vacuum to sparse is marked by an abrupt increment in the average electron density value.

The calculated interspace size increases with time in our simulation system. Fig. 4.5 shows a plot of interspace size μm versus time fs. At t = 150 - 500 fs , the interspace size vary from 0.19 to 0.5 μm and this is indicating the growth of the periodic nanograting structure with time evolution.
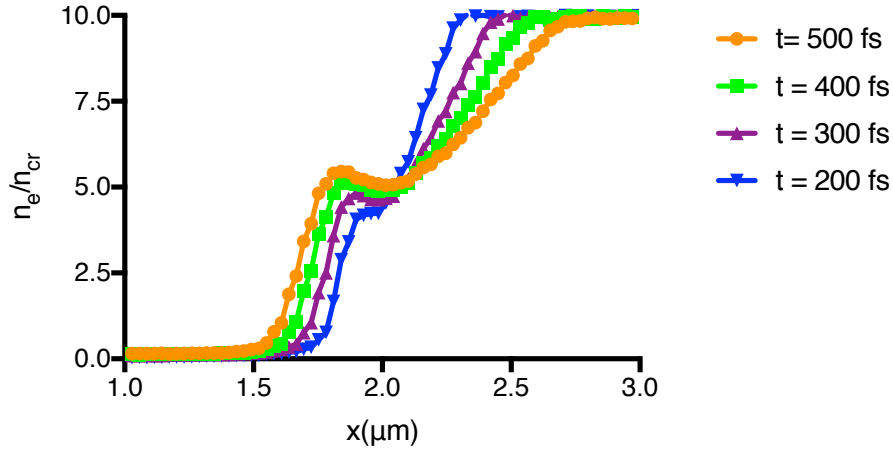
FIGURE 4.3: Average electron density n_e/n_{cr} versus distance x μm with different density at (a) t = 200, (b) t = 300, (c) t = 400, and (d) t = 500 fs. The blue, purple, green, and orange curves represent the value calculated at (a) t = 200, (b) t = 300, (c) t = 400, and (d) t = 500 fs, respectively. This graph shows how is the electron density is increase with time increasing in the intermediate area. The recorded growth in the intermediate area are the reason for forming the periodic nanograting structure under the effect of the physical phenomena in this area.
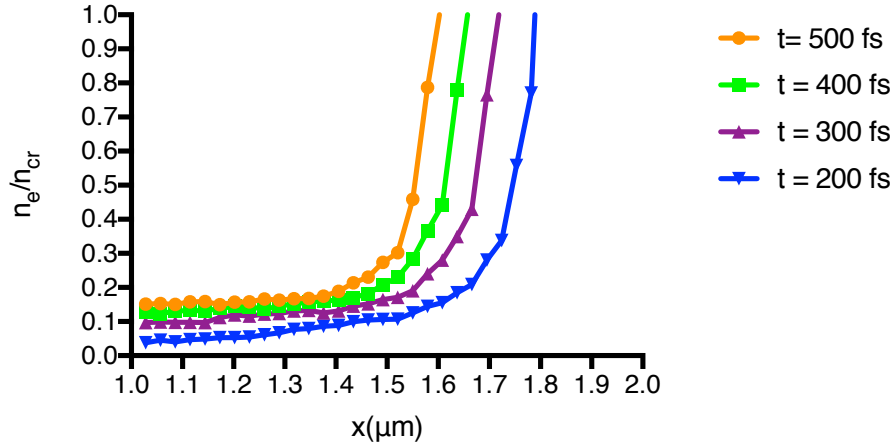
FIGURE 4.4: Average electron density n_e/n_{cr} versus distance x μm within the specific region from x = 1 μm to 2 μm. Curves in blue, purple, green, and orange graphs, represent the average densities at (a) t = 200, (b) t = 300, (c) t = 400, and (d) t = 500 fs, respectively. Through this graph we can record the initial transition from vacuum to sparse.

4.4   Surface plasma wave and its roles in formation mechanism

SPWs were first described by J. Zenneck in 1907 [58]. In general, SPWs exist along the boundary between two different medium that can be either isotropic or anisotropic (in our case sparse-intermediate plasma interface). Moreover, SPWs can be confined to narrow areas and travel along the interface of the two medium also it decay exponentially in a direction perpendicular to the boundary of the two medium. The dispersion relation is the most important techniques used to determine the required conditions to form SPWs.
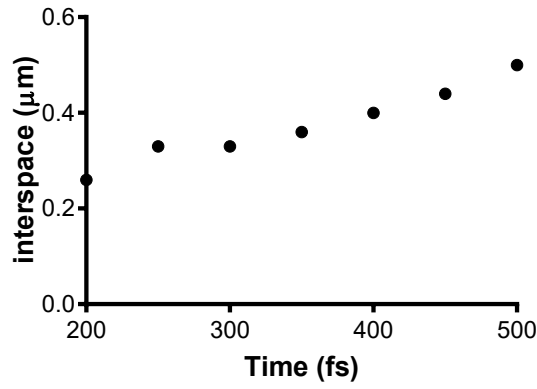
FIGURE 4.5: measured interspace versus time. At t = 200, 250, 300, 350, 400, 450, and 500 fs, the measured interspace equals 0.26, 0.33, 0.33, 0.36, 0.4, 0.45, and 0.5 μm, respectively. We can calculate the measured interspace directly from the electron density profile.

To this end, two conditions must be met [59]. The dielectric constants of the sparse and the intermediate areas (ε_{sparse} and ε_{inter}, respectively) must satisfy the following conditions:

$$\varepsilon_{sparse} \cdot \varepsilon_{inter} < 0, \tag{4.1}$$

$$\varepsilon_{sparse} + \varepsilon_{inter} < 0. \tag{4.2}$$

An additional condition assumed in our study to enable the electrons at the surface of the interface to be oscillate with the frequency of the laser electric field is;

$$\omega_{sp} = \omega_L \tag{4.3}$$

where ω_{sp} is the frequency of surface plasma wave while ω_L is the laser frequency. Herein, we study the real values of the dispersion relation of the SPW. The dielectric constant of the sparse area ε_{sparse} is assumed to range from 0.9 to 0.1 when n_{sparse} ranging from 0.1 to 0.9. whereas, the dielectric constant of the intermediate area will always be $\varepsilon_{inter} < 1$ because n_{inter} is greater than 1. Since the dielectric constant is well known as a function of the electron density as following:

$$\varepsilon = 1 - \frac{\omega_{pe}^2}{\omega_L^2} = 1 - \frac{n_e}{n_{cr}}. \tag{4.4}$$

The derivation of the dispersion relation of the SPW is provided separately in the Appendix A. The well known SPW dispersion relation is given as follows:

$$\mathbf{k}_{sp} = \mathbf{k}_L \sqrt{\frac{\varepsilon_{sparse} \cdot \varepsilon_{inter}}{\varepsilon_{sparse} + \varepsilon_{inter}}}, \tag{4.5}$$

where k_L is the wavenumber of the laser beam.

The wavelength of the SPW can be easily calculated as a function of the electron density as follows;

$$\frac{\lambda_{sp}}{\lambda_L} = \sqrt{[2 - (\frac{n_{sparse} + n_{inter}}{n_{cr}})]/[(1 - \frac{n_{sparse}}{n_{cr}})(1 - \frac{n_{inter}}{n_{cr}})]}. \tag{4.6}$$

The normalized wavelength of SPW given by Eq. 4.6 increases with the increment of n_{inter} and n_{sparse}. In Fig. 4.6, a relational graph has been drawn to explain the effect of both n_{sparse} and n_{inter} on the normalized wavelength λ_{sp}/λ_L.
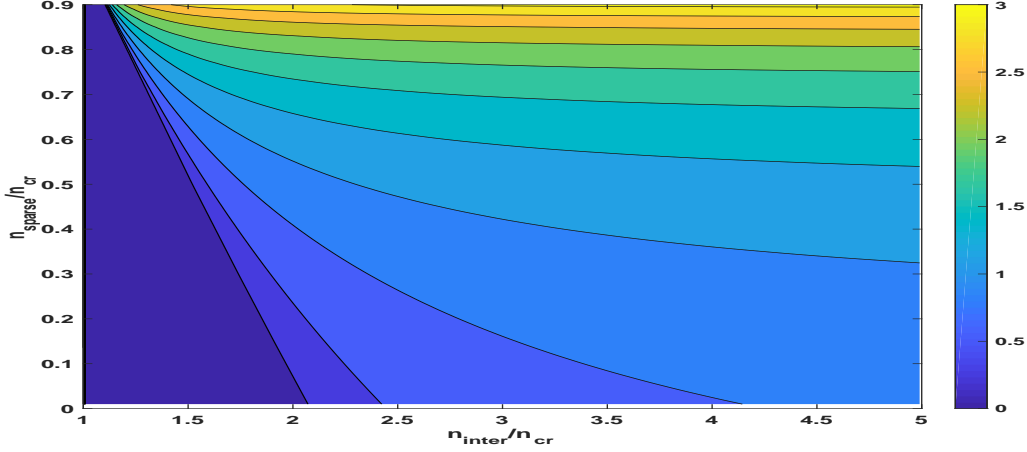
FIGURE 4.6: Wavelength of SPW with different density values. The graph is drawn for the range $n_{sparse} = 0 \sim 0.9 \; n_{cr}$ and $n_{inter} = 1 \sim 5 \; n_{cr}$.

To understand how is the SPW acts on the periodic nanograting structure formation mechanism, we have to recall the ponderomotive force $\mathbf{F_{SPW}}$ effect behind the SPW. The mechanism of SPW generation is based on the collective behavior of the excited electrons in the y-direction due to the electric field component of the laser beam. The bidirectional collective behavior of the electrons in both positive and negative y-axis, leads to SPW propagation near to the interface, producing the so- called standing wave. The standing wave's $\mathbf{F_{SPW}}$ plays a major role in forming seeds or tips for the development of periodic nanograting structures at early stages since it is repeated each $\lambda_{sp}/2$ according to Eq. 4.7. A complete explanation on how to derive $\mathbf{F_{SPW}}$ in the Eq. 4.7 is given in Appendix B. The ponderomotive force of the SPW is shown as follows:

$$\mathbf{F_{SPW}} = -\frac{\omega_{pe}^2}{\omega_{sp}^2} k_{sp} \varepsilon_o \mathbf{E_o}^2 \sin(2k_{sp}y). \tag{4.7}$$

To find the interface position, we need to calculate the balanced density n_{ba} from the laser pressure $\mathbf{P_L}$ and the plasma pressure $\mathbf{P_{Plasma}}$.

$$\mathbf{P_L} = 2I_L/c = 6.67I_L[10^{16}W/cm^2][Mbar], \tag{4.8}$$

$$\mathbf{P_{plasma}} = 1.79\frac{n_{ba}}{n_{cr}}T_e[keV]/\lambda_L^2[\mu m][Mbar]. \tag{4.9}$$

The balance of pressure $\mathbf{P_L} = \mathbf{P_{plasma}}$ [60, 61] allows us to find $n_{ba} = 2.384\ n_{cr}$. With the help of electron density (n_e/n_{cr}), we can accurately determine the position at which n_{ba} is along x-axis and consider it as the interface location. Fig. 4.7 is a graph showing two data sets for the electron density (n_e/n_{cr}) distribution along the x-axis at time t = 500 fs. With this information, we can find the interface position x_i.
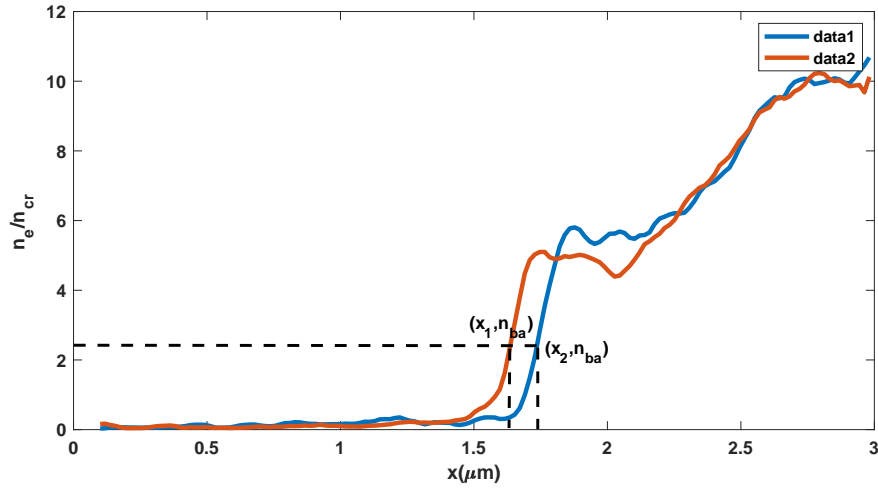
FIGURE 4.7: Schematic graph showing the electron density distribution along the x-axis at time t = 500 fs. We used this graph to show the position of the interface.

The relation between the interface position and the time is illustrated in Fig. 4.8. Based on relation interface position with time from 200 to 500 fs, we can observe that the interface position expands towards the left-hand side of the x-axis in a very slow rate, i.e., $\sim 0.186\ \mu m$ per 300 fs. Besides, the relation in Fig. 4.8 will help in our future n_{sparse} and n_{inter} calculation.
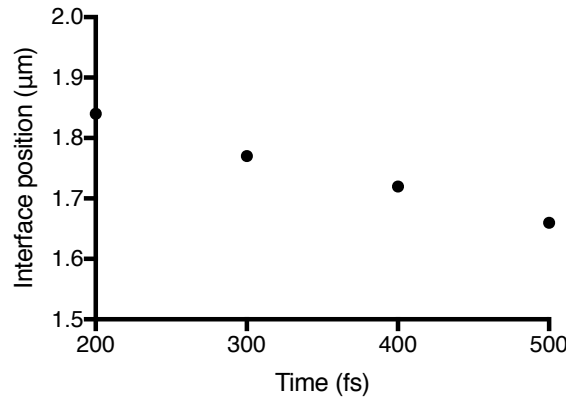
FIGURE 4.8: Interface position through x-axis versus time. The points represent the position of the interface on the x-axis with time evolution for average density.

Next, we show a mean of obtaining n_{sparse} and n_{inter} from our simulation system to further confirm the existence of the SPW. The basic principle for obtaining the electron densities n_{sparse} and n_{inter} relies on the corrected place to pick up the required densities. According to the theory of the SPW

TABLE 4.1: Shows the time effects on , n_{inter}/n_{cr}, n_{sparse}/n_{cr}, λ_{sp}/λ_L, theoretical interspace $\lambda_{sp}/2$, and the measured interspace respectively. Using of n_{inter}/n_{cr} and n_{sparse}/n_{cr} are helping in calculating the dispersion relation of SPW and the theoretical interspace $\lambda_{sp}/2$. We compared between the theoretical interspace and the measured interspace in order to confirm the validity of our calculation.

Time (fs)	n_{inter}/n_{cr}	n_{sparse}/n_{cr}	λ_{sp}/λ_L	$\lambda_{sp}/2(\mu m)$	measured interspace (μm)
200	4.58	0.10	0.91	0.36	0.26
300	4.83	0.14	0.95	0.38	0.33
400	5.26	0.17	0.98	0.39	0.40
500	5.51	0.19	1.00	0.40	0.50

[62], the required densities n_{sparse} and n_{inter} should be measured along the interface between sparse-intermediate media.

The procedure for calculating n_{sparse}/n_{cr} and n_{inter}/n_{cr} is proposed as follows:

1. Based on the electron density raw data from FISCOF2 we will begin to calculate n_{inter}/n_{cr} and n_{sparse}/n_{cr}.

2. The noise in the data need to be eliminated before calculating n_{inter}/n_{cr} and n_{sparse}/n_{cr}. We will smooth the raw data by using the moving average method of order 3 [63].

3. After smoothing the electron density data, we find the position of interface x_i via the analysis shown in Fig. 4.7. for example at t = 500 fs, there are 213 curves and that mean there are 213 value of x_i since i = 1, 2, 3,..,etc.

4. After determining x_i, we can determine x_{sparse} as the first local minima on the left hand side and x_{inter} as the first local maxima on the right hand side of x_i.

5. Using x_{sparse} and x_{inter}, we can find n_{inter} and n_{sparse} over all raw data.

6. After finding all n_{inter} and n_{sparse} values, we can calculate the average values of n_{inter} and n_{sparse} we can use them to calculate the inverse of dispersion relation (wavelength of SPW) λ_{sp}/λ_L , theoretical interspace (half of the SPW wavelength) $\lambda_{sp}/2$, and the measured interspace.

Table 4.1 summarizes the effect of time on n_{inter}/n_{cr}, n_{sparse}/n_{cr}, and λ_{sp}/λ_L, theoretical interspace $\lambda_{sp}/2$, and the measured interspace respectively.

Fig. 4.9 Shows a comparative graph between the theoretical and the measured interspace size. We can observe two colored lines; the blue and the purple represent the theoretical and measured interspace with time variation, respectively. Fig. 4.9 shows that at t = 200, 300, 400, and 500 fs the theoretical interspace = 0.36, 0.38, 0.40, and 0.40 μm while the calculated interspace = 0.26, 0.33, 0.4, and 0.50 μm . The previous results show a great consistent between the theoretical and the calculated interspace.
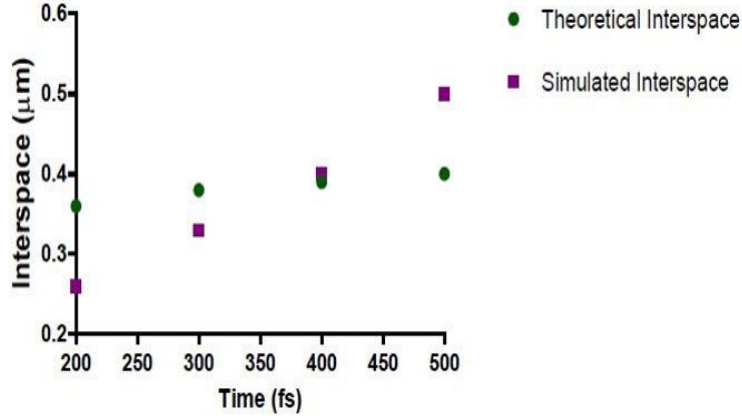
FIGURE 4.9: Comparison between the theoretical (continuous line), and the measured interspace (dashed line) with time evolution.

4.5   Oscillating two stream instability and its roles in the formation mechanism

OTS instability is a process by which a long wavelength pump wave excites short electrostatic waves accompanied by increasing density perturbation. OTS instability can occur when $\omega_L < \omega_{pe}$ where ω_L is the laser frequency while, ω_{pe} is the electron plasma frequency [4]. To explain how is SPW acts together with OTS instability in the growth of periodic nanograting structures, we should explain the effect of OTS instability growth rate γ_{ots}/ω_L on the periodic nanograting structure in details.

Since there is a density perturbation in the intermediate area of the plasma due to the $\mathbf{F_{SPW}}$ of SPW and because the system is under the effect of the laser electric field $\mathbf{E_L}$ on the interface between the sparse-intermediate area, the electrons will move in a direction opposite to the $\mathbf{E}_L$, producing nonlinear electric field $\mathbf{E}_1$. In contrast, ions do not move on a similar time scale of ω_L and density ripples causes a charge separation. The electrostatic charges create a field $\mathbf{E}_1$ that oscillates at frequency ω_L. A new nonlinear ponderomotive force related to OTS $\mathbf{F_{NL}}$ governs the total field $\mathbf{E_L} + \mathbf{E_1}$, as pointed out by Eq. 4.10 as follows

$$\mathbf{F_{NL}} = -\frac{\omega_{pe}^2}{\omega_L^2}\varepsilon_o\frac{\left\langle (\mathbf{E_L} + \mathbf{E_1})^2 \right\rangle}{2}, \tag{4.10}$$

$\mathbf{F_{NL}}$ never cancelled since E_1 changes its sign according to E_L. However, $\mathbf{F_{NL}}$ cancels only at the tips and troughs of n_1 and it is large where ∇n_1 is large. This spatial distribution causes $\mathbf{F_{NL}}$ to push the electrons from a low density region to a high density region. The resulting DC electric field drags the ions along also, and the density perturbation grows. The threshold value of $\mathbf{F_{NL}}$ is the value just sufficient to overcome the pressure $\nabla n_{i1}(kT_e + kT_i)$ which tends to smooth the density. This is called OTS because the sloshing electrons have a time-averaged distribution function which is double peaked the electron density regions and this is the reason for growing up the tips.
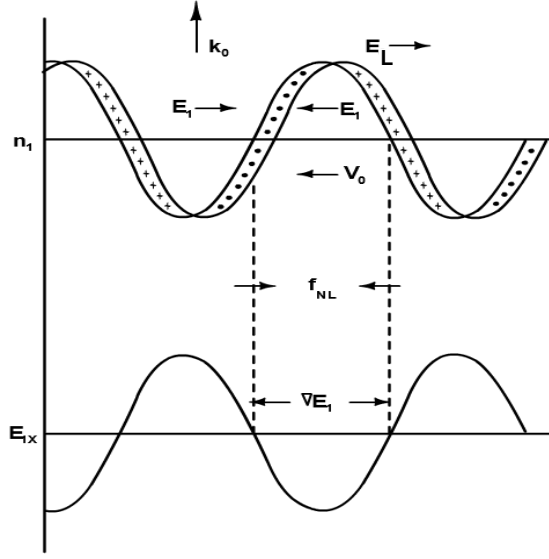
FIGURE 4.10: Schematic shows the oscillating two stream instability process according to reference
[4].

Eq. 4.11 was employed to calculate the growth rate of OTS instability (γ_{ots}/ω_L). The process of
the OTS see Fig. 4.10 is explained in several textbooks, and the details on the derivative to find the
equation of (γ_{ots}/ω_L) is all collected in Appendix C.

Assume Q = ω^2 , since; $\omega = \omega_{real} + i\gamma_{ots}$ we used the imaginary part of ω to define the growth rate
γ_{ots}/ω_L. The plasma and laser parameters which affects on γ_{ots}/ω_L can be expressed as follows:

$$Q^3 - (2 + \widehat{\omega}_{pe}^2)Q^2 + (1 + 2\widehat{\omega}_{pe}^2 - 2\widehat{k}_{sp}^2 a_o^2 \frac{m_e}{M_i})Q - (\widehat{\omega}_{pe}^2 + 2\widehat{k}_{sp}^2 a_o^2 \frac{m_e}{M_i}) = 0, \qquad (4.11)$$

where a_o is the laser parameter and it equals to $a_o = eE_L/m_e c\omega_L = 0.85\lambda_L\sqrt{I_L}$ (I_L is the laser
intensity in $[10^{18}W/cm^2]$). $\widehat{k}_{sp} = \frac{k_{sp}}{k_L}$ and $\widehat{\omega}_{pe}^2 = \frac{n_{inter}}{n_{cr}}$ are the normalized wavenumber and the
normalized electron plasma frequency by the laser frequency, respectively. Please note that, $\widehat{\omega}_{pe}^2$ and
$\widehat{k}_{sp}$ can be calculated from table 4.1. The electron to ion mass ratio is defined as $\frac{m_e}{M_i}$ and it is equal
0.0087.

In Fig. 4.11 the behavior of the growth rate γ_{ots}/ω_L versus the normalized electron plasma frequency
$\widehat{\omega}_{pe}$ can be analyzed. With increasing the electron density, the growth rate begins to decrease gradually
after reaching its maximum at a period from 1 to 2 n_{cr}. We can recall the density at which the γ_{ots}/ω_L
recorded its highest value at (n_{con}).

At t = 300 fs γ_{ots}/ω_L is equal to 0.0034 and it decreases as time increases. The existence of γ_{ots}/ω_L
helped the growth of the periodic nanograting structure. For instance, by assuming γ_{ots} T = 1 (where
T: is the required time to observe growth rate of OTS), if $\gamma_{ots}/\omega_L = 0.004$, then T equals 100 fs, that
means the grow rate γ_{ots}/ω_L is occur within the simulation time of our case.
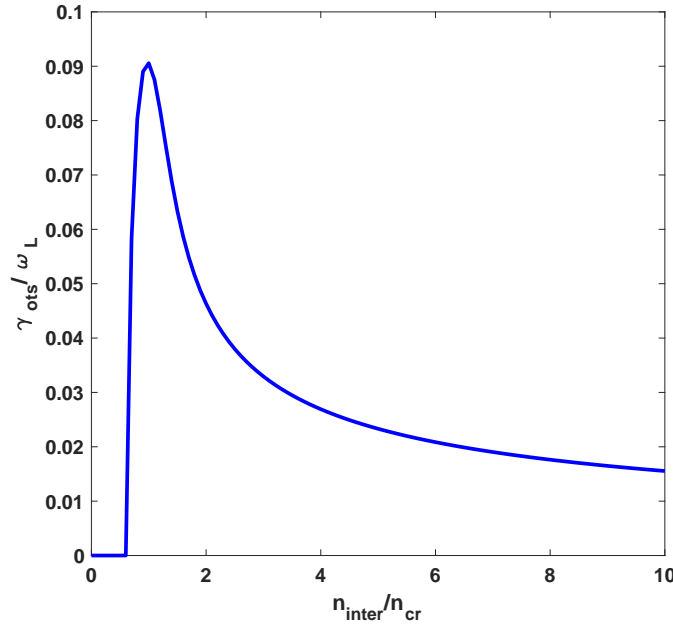
FIGURE 4.11: Growth rate γ_{ots}/ω_L versus density $\widehat{\omega}_{pe}^2$. The growth rate increases as the electron density increase up until it reaches its maximum followed by a decrement with increasing the density.

TABLE 4.2: Shows the time effects on $\widehat{\omega}_{pe}^2$, $\widehat{k}_{sp}^2$, and γ_{ots}/ω_L respectively. The normalized electron plasma frequency ($\widehat{\omega}_{pe}^2$) is increasing over time while the normalized wavenumber $\widehat{k}_{sp}^2$ and the growth rate (γ_{ots}/ω_L) are decreasing with time evolution

Time(fs)	$\widehat{\omega}_{pe}^2$	$\widehat{k}_{sp}^2$	γ_{ots}/ω_L
200	4.58	1.0989	0.0037
300	4.83	1.0526	0.0034
400	5.26	1.0204	0.0031
500	5.51	1.0000	0.0030

Table 4.2 shows the effect of time with the measured values of $\widehat{\omega}_{pe}^2$ $\widehat{k}_{sp}^2$, and γ_{ots}/ω_L, respectively. We can observe that the density $\widehat{\omega}_{pe}^2$ is increasing with time evolution, while the wavenumber $\widehat{k}_{sp}^2$ and growth rate γ_{ots}/ω_L decreases with time.

In Fig. 4.12 the behavior of the growth rate γ_{ots}/ω_L over time shows a decreasing values of the growth rate but it never reaches zero within the time frame considered. The periodic nanograting structure enlarges with time due to existence of the OTS.

4.6   Conclusion

In chapter 4, the formation mechanism of the periodic nanograting structures by non-relativistic laser pulses is studied by using a simulation of its growth using a 2D PIC code (FISCOF2). The SPW and the OTS phenomena have a significant role in explaining the formation mechanism. When the laser
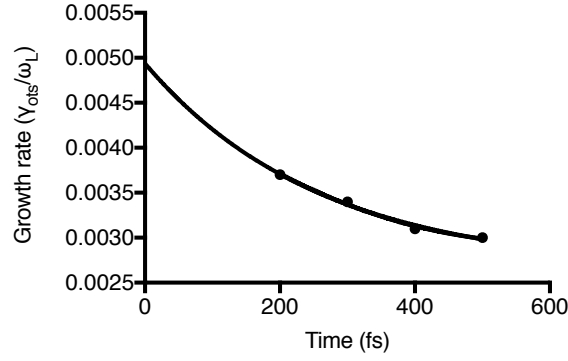
FIGURE 4.12: Variation in growth rate γ_{ots}/ω_L versus time evolution. We can observe that γ_{ots}/ω_L is decreasing over time t but it never reaches zero.

beam irradiates boundary between the vacuum-plasma interface, the mechanism of SPW generation is considered.

Based on the collective behavior of the excited electrons in the y-direction due to the electric field component of the laser beam. The bidirectional collective behavior of the electrons in both positive and negative y-axis, leads to SPW propagation near to the interface, producing the so-called standing wave. The standing wave's $\mathbf{F_P}$ plays a significant role in forming seeds or tips for the development of periodic nanograting structures. The OTS instability affects the formed tips and grows them up to form complete structure from the periodic nanograting.

The electron density profile successfully showed growth enhancement over time. At t = 500 fs, periodic nanograting structures form at the interface of the sparse–intermediate area, with an interspace size of 0.5 μm. The measured interspaces sizes were found to agree with the theoretical interspace.

Chapter 5

Summary

This thesis presents an ample study on the formation mechanism of the periodic nanograting structure by using Particle In Cell code (FISCOF2). This thesis contains five chapters. The first and the second chapters describe the motivation and background of the work in addition to the main plasma physics models, which are used to introduce and describe plasma physics from different points of view such as the kinetic model, the single-particle mode, the fluid model, and the MHD model.

In Chapter 3, the formation mechanism of the periodic nanograting structure is studied by using FISCOF2. The laser beam with an intensity of 10^{18} W/cm$^2 - \mu$m^2 irradiates the mimic target's plasma interface for about 500 fs. The Weibel instability theory explains the enhancements of the magnetic field and electron current density in our interface with time evolution. Later, the Weibel instability theory shows how the magnetic field, together with the electron current density, creates the periodic nanograting structure with time evolution. The simulation framework in Chapter 3 is formed from two regions: The first region is the so-called mimic plasma, which resizes along with the x-axis from 0 to 2 μm and along the y-axis from -3.6 to 3.6 μm. Electron density in the mimic plasma is assumed to be 0.7 n_{cr}, where n_{cr} is the critical density for a laser wavelength of 800 nm. The second region is the so-called target plasma with a density of 10 n_{cr} that resides behind the mimic plasma and expands along the x-axis from 2 to 12 μm and along the y-axis from -3.6 to 3.6 μm. The mimic plasma's thickness is about 2 μm while the target plasma is about 10 μm along the x-direction of x-y plane. The laser beam is injected onto the surface from the left side of the simulation system. The laser beam's intensity of $I = 10^{18}$ W/$cm^2 - \mu m^2$, laser wavelength of $\lambda_L = 800$ nm, and laser rise time of $\tau = 15$ fs irradiates continuously onto the mimic-target interface at normal incidence. We used hydrogen plasma with electron temperature $T_e = 1$ keV, ion temperature $T_i = 0.1$ keV, and the ion-electron mass ratio $M_i/m_e = 1836$ in order to accelerate the simulation process. The periodic nanograting structure has been clearly self-organized at the boundary between the mimic-target plasma interface at t = 200 fs, as shown in Fig. 3.2. At t = 250 fs, 13 tips from the periodic nanograting structure are formed along the y-axis from -3.0 to 3.0 μm, and the average interspace size of 0.46 μm is shorter than the laser wavelength. The periodic nanograting structures are observed at

y = -0.8, -0.6, -0.2, 0.3, and 0.9 μm in the electron density profile where the positive x-component of the electron current density J_{xe} exists. Furthermore, the positive and the negative z-component values of the enhanced magnetic field B_z are shown in between the above positions. For example at y = 0.3 μm, the positive z-component of B_z exists at y = 0.5 μm while the negative z-component of B_z exists at y = 0.1 μm. The above description shows the consistency between the enhanced magnetic field and the electron current density, which leads to producing a periodic nanograting structure and confirming the existence of Weibel instability.

In chapter 4, the formation mechanism of the periodic nanograting structure is studied by using FISCOF2. The laser beam of intensity 10^{16} W/cm^2 $- \mu m^2$ irradiates the plasma for about 500 fs. The surface plasma wave and the oscillating two-stream instability have been considered the formation mechanism of the periodic nanograting structure. The framework in chapter 4 is slightly different from chapter 3. In the vacuum-target plasma interface, the framework of the present simulation system is formed by one limited region, which is surrounded by vacuum everywhere. This area contains (dense) target plasma with the assumed electron density of value n_{target} of 10 n_{cr}, where n_{cr} is the critical density of the laser beam of wavelength 800 nm. The target plasma resides on the x-axis in the range 2 to 12 μm and on the y-axis in the range – 10 to 10 μm. We consider a nonrelativistic laser beam with a flat-top profile shape being continuously irradiated onto the target at a normal incidence for about 500 fs. The laser beam parameters are defined in our simulation framework as follows: intensity of $I = 10^{16}$ $W/cm^2 - \mu m^2$, wavelength of $\lambda_L = 800$ nm, full wave half maximum of $\phi_{FWHM} = 10$ μm, and rise time $\tau = 5$ fs. Based on the collective behavior of the excited electrons in the y-direction due to the electric field component of the laser beam. The bidirectional collective behavior of the electrons in both positive and negative y-axis leads to form SPW and propagation near the interface, producing the so-called standing wave. The ponderomotive force of the standing wave plays a significant role in forming seeds or tips. For enlarging the periodic nanograting structures, the oscillating two stream instability shows a role in growing the tips up to form the periodic nanograting structure. At t = 500 fs, periodic nanograting structures form at the interface of the sparse-intermediate area, with an interspace size of 0.5 μm, which agrees with the theoretical model.

Appendix A

Derivative of Dispersion Relation of Surface Plasma Wave

Consider that ε_{sparse} , ε_{inter}: are the permittivity of the sparse and the intermediate plasma, respectively in our simulation system. The electric field laser beam is a p-polarized wave propagates in the y-direction. There is no z dependence. We describe the fields in the media (1) and (2) as follows;

$$x > 0 \qquad \mathbf{H_2} = (0, 0, H_{z2}) \exp i(k_2 x - \omega t) \tag{A.1}$$

$$\mathbf{E_2} = (E_{x2}, E_{y2}, 0) \exp i(k_2 x - \omega t) \tag{A.2}$$

$$x < 0 \qquad \mathbf{H_1} = (0, 0, H_{z1}) \exp i(-k_1 x - \omega t) \tag{A.3}$$

$$\mathbf{E_1} = (E_{x1}, E_{y1}, 0) \exp i(-k_1 \mathbf{x} - \omega t). \tag{A.4}$$

These fields have to fulfill Maxwell equations:

$$c \, \nabla \times \mathbf{B} = 4\pi \mathbf{J} + \frac{\partial \mathbf{E}}{\partial t}, \tag{A.5}$$

$$c \, \nabla \times \mathbf{E} = -\frac{\partial \mathbf{B}}{\partial t}, \tag{A.6}$$

$$\nabla \cdot \mathbf{E} = 4\pi e(n_i - n_e), \tag{A.7}$$

$$\nabla \cdot \mathbf{B} = 0. \tag{A.8}$$

Together with the continuity relations

$$E_{x1} = E_{x2}, \tag{A.9}$$

$$H_{z1} = H_{z2}, \tag{A.10}$$

$$\varepsilon_1 E_{y1} = \varepsilon_2 E_{y2}. \tag{A.11}$$

From Eq. A.9 and A.10 follows the continuity of

$$k_{x1} = k_{x2} = k_x. \tag{A.12}$$

Eq. A.5 gives

$$\frac{\partial H_{zi}}{\partial x} = -\varepsilon_i E_{yi} \frac{\omega}{c}, or$$

$$k_{x1} H_{z1} = \frac{\omega}{c} \varepsilon_i E_{y1}, \tag{A.13}$$

$$k_{x2} H_{z2} = -\frac{\omega}{c} \varepsilon_i E_{y2}. \tag{A.14}$$

Eq. A.13 together with Eqs. A.9 and A.10 yield

$$H_{z1} - H_{z2} = 0$$

$$\frac{k_{x1}}{\varepsilon_1} H_{z1} + \frac{k_{x2}}{\varepsilon_2} H_{z2} = 0.$$

To obtain a solution, the determinant has to be zero

$$D_o = \frac{k_{x1}}{\varepsilon_1} + \frac{k_{x2}}{\varepsilon_2} = 0.$$

This is the dispersion relation SPW in the system. Further we get Eqs. A.3, A.4, and A.11:

$$k_y^2 + k_{xi}^2 = \varepsilon_i \left(\frac{\omega}{c}\right)^2.$$

And the final and common shape is :

$$k_y = \left(\frac{\omega}{c}\right) \sqrt{(\varepsilon_1 \varepsilon_2)/(\varepsilon_1 + \varepsilon_2)}. \tag{A.15}$$

Appendix B

Derivative of Ponderomotive Force of Surface Plasma Wave

In physics, a ponderomotive force is a nonlinear force that a charged particle experiences in an inhomogeneous oscillating electromagnetic field. The ponderomotive force has been derived in many books [4, 36] after studying the equation of motion of the electrons in the oscillating electric field (E), the ponderomotive force is well known as $\mathbf{F_{SPW}}$ as follows:

$$\mathbf{F_{SPW}} = -\frac{\omega_{pe}^2}{\omega_L^2} \frac{\varepsilon_o}{2} \nabla \left\langle E^2 \right\rangle. \tag{B.1}$$

We are able to define the effect of the ponderomotive force of the SPW and study how is this force causes the formation of the seeds of the periodic nanograting structure. Let's us assume that E_T is the total electric field along the interface between sparse and intermediate area as follows:

$$E_T = \mathbf{E_p} + \mathbf{E_n}, \tag{B.2}$$

where $\mathbf{E_p}$ and $\mathbf{E_n}$ are the bi–directional electric field through the positive and the negative y-direction due to electron motion. We had to know that the electron motion are bounded to the boundary between the spare-intermediate interface. The equation form of both $\mathbf{E_p}$ and $\mathbf{E_n}$ will be define as follows:

$$\mathbf{E_p} = \mathbf{E_o} \cos(\omega_{sp} t - k_{sp} y), \tag{B.3}$$

$$\mathbf{E_n} = \mathbf{E_o} \cos(\omega_{sp} t + k_{sp} y + \pi). \tag{B.4}$$

By considering the phase difference equal π between $\mathbf{E_n}$ and $\mathbf{E_p}$, E_T will be redefine as follows:

$$E_T = \mathbf{E_o} \cos(\omega_{sp}t - k_{sp}y) + \mathbf{E_o} \cos(\omega_{sp}t + k_{sp}y + \pi),$$

$$E_T = 2E_o \sin(\omega_{ps}t) \sin(k_{sp}y),$$

$$E_T^2 = 2\mathbf{E_o}^2 \sin^2(\omega_{sp}t) \sin^2(k_{sp}y). \tag{B.5}$$

The time average of the total electric field E_T^2 will be calculated as follows:

$$\left\langle E_T^2 \right\rangle = \frac{4\mathbf{E_o}^2}{T} \int_{t=0}^{t=T} \sin^2(\omega_{sp}t) \sin^2(k_{sp}y)dt,$$

since $\sin^2(\omega_{sp}t)$ can be rewrite as $[\frac{1}{2} - \frac{1}{2}\cos(2\omega_{sp}t)]$

$$\left\langle E_T^2 \right\rangle = \frac{4\mathbf{E_o}^2}{2T} \sin^2(k_{sp}y) \int_{t=0}^{t=T} dt - \frac{4\mathbf{E_o}^2}{2T} \sin^2(k_{sp}y) \int_{t=0}^{t=T} \cos(2\omega_{sp}t)dt,$$

$$\left\langle E_T^2 \right\rangle = 2\mathbf{E_o}^2 \sin^2(k_{sp}y), \tag{B.6}$$

or

$$\left\langle E_T^2 \right\rangle = \mathbf{E_o}^2 - E_o^2 \cos(2k_{sp}y),$$

by taking ∇ derivative to $\left\langle E_T^2 \right\rangle$ we will get:

$$\mathbf{F_{SPW}} = -\frac{\omega_{pe}^2}{\omega_{sp}^2} k_{sp}\varepsilon_o \mathbf{E_o}^2 \sin(2k_{sp}y). \tag{B.7}$$

From Eq. B.7 we can understand that the $\mathbf{F_{spw}}$ repeated itself each $\lambda_{sp}/2$ and that is the reason for forming the seeds of the periodic structure in the early time within our simulation system.

Appendix C

Derivative of Growth Rate for Oscillating Two Stream Instability

Let us consider the temperature of electrons and ions be T_e and T_i while the collision rate of the electrons and ions be ν_e and ν_i. Assume that T_e, T_i, ν_e and ν_i all vanish, the ion fluid then obeys the low frequency equations as follows;

$$Mn_o \left(\frac{\partial \mathbf{v}_{il}}{\partial t} \right) = en_o \mathbf{E}_L = \mathbf{F_{NL}}, \tag{C.1}$$

$$\frac{\partial n_{il}}{\partial t} = n_o \frac{\partial \mathbf{v}_{il}}{\partial x} = 0, \tag{C.2}$$

please consider that, in case of spatial homogeneous, we are able to analyze with Fourier in space and replace $\partial/\partial x$ by ik.

where $\mathbf{F_{NL}}$ is the ponderomotive force and it is well defined as ;

$$\mathbf{F_{NL}} = -\frac{\omega_{pe}^2}{\omega_L^2} \varepsilon_o \frac{\left\langle \mathbf{E}_L + \mathbf{E}_1 \right\rangle^2}{2}. \tag{C.3}$$

Therefore, the time derivative of Eq. C.2 together with Eq. C.3 gives:

$$\frac{\partial^2 n_{il}}{\partial t^2} + \frac{ik}{M} \mathbf{F_{NL}} = 0. \tag{C.4}$$

To find $\mathbf{E}_1$ from Eq. C.3, we must consider the electron equation of motion of the electrons which given by;

$$m \left(\frac{\partial \mathbf{v}_e}{\partial t} + \mathbf{v}_e \frac{\partial}{\partial x} \mathbf{v}_e \right) = -e(\mathbf{E}_L + \mathbf{E}_1), \tag{C.5}$$

where $\mathbf{E_1}$ is the electron electric field under the effect of the laser electric field $\mathbf{E_L}$. It is found that $\mathbf{E_1}$ related to the density by using Poisson's equation as follows:

$$ik\varepsilon_o\mathbf{E}_1 = -e\mathbf{v}_e n_e \tag{C.6}$$

Another understanding should be considered for the quantities $\mathbf{E}_1$, $\mathbf{v}_e$, and n_e that each of them have two parts: a high frequency part, in this case the electrons move independently of the ions. In case of a low frequency part, electrons move along with the ions in a quasi-neutral manner. For lowest order, the motion is a high-frequency one in response to the spatially uniform field $\mathbf{E}_L$ as follows:

$$\frac{\partial \mathbf{v}_{eo}}{\partial t} = -\frac{e}{m_e}(\mathbf{E}_L) = -\frac{e}{m_e}(\mathbf{E}_o \cos\omega_o t), \tag{C.7}$$

linearizing about this oscillating equilibrium, we have the next order of:

$$\frac{\partial \mathbf{v}_{e1}}{\partial t} + ik\mathbf{v}_{eo}\mathbf{v}_{e1} = -\frac{e}{m_e}\mathbf{E}_1 = -\frac{e}{m_e}(\mathbf{E}_{1h} + \mathbf{E}_{1l}), \tag{C.8}$$

where the subscripts (h) and (l) denote the high and low frequency parts. The first term of the high frequency velocity $\mathbf{v_{eh}}$ given by:

$$\frac{\partial \mathbf{v}_{eh}}{\partial t} = -\frac{e}{m_e}\mathbf{E}_{1h} = \frac{e^2 n_{eh}}{ikm_e\varepsilon_o}, \tag{C.9}$$

where we have used Eq. C.6. The low frequency part of Eq C.8 is given by:

$$ik\mathbf{v}_{eo}\mathbf{v}_{eh} = -e\mathbf{E}/m_e. \tag{C.10}$$

The right hand side of the above Eq. C.10 represents the ponderomotive term used in Eq. C.3 to derive the ion waves. The right hand side results from the low frequency beat between $\mathbf{v}_{eo}$ and $\mathbf{v}_{eh}$ while the left hand side related to the electrostatic part of the ponderomotive force expression Eq. C.3 . The electron continuity equation is defined by:

$$\frac{\partial n_{el}}{\partial t} + ik\mathbf{v}_{eo}n_{e1} + ik\mathbf{v}_{e1}n_o = 0, \tag{C.11}$$

since our consideration is in the high-frequency part of Eq. C.11, the middle term only shows the low-frequency density n_{el} which can beat with $\mathbf{v}_{eo}$ to give a high-frequency term. With rejecting phenomena near $2\omega_L$ and higher harmonics, we can replace n_{el} with n_{il} due to quasi-neutrality so we have:

$$\frac{\partial n_{eh}}{\partial t} + ik\mathbf{v}_{eh}n_o + ik\mathbf{v}_{eo}n_{il} = 0. \tag{C.12}$$

With applying time derivative, we neglect $\frac{\partial n_{i1}}{\partial t}$ and we use Eqs. C.7 and C.9 to get:

$$\frac{\partial^2 n_{eh}}{\partial t^2} + \omega_{pe}^2 n_{eh} = \frac{ike n_{il}\mathbf{E}_o}{m_e}. \tag{C.13}$$

Let n_{eh} vary as $\exp -i\omega t$

$$(\omega_{pe}^2 - \omega^2)n_{eh} = \frac{ike}{m_e}n_{i1}\mathbf{E}_o \tag{C.14}$$

to solve the problem exactly we will use Eq. C.14 with the following equation;

$$\frac{\partial^2 n_{i1}}{\partial t^2} = \frac{k^2 e^2}{2M_i m_e}n_{eh}\frac{\mathbf{E}_o^2 n_{i1}}{\omega_{pe}^2 - \omega_o^2} \tag{C.15}$$

Eq. C.14 and Eq. C.15 will be considered as two harmonic oscillators to each other and will be handle same as simple harmonic oscillator.

The equation of motion for a simple harmonic oscillator x_1:

$$\frac{d^2\mathbf{x_1}}{dt^2} + \omega_1^2\mathbf{x_1} = 0 \tag{C.16}$$

where ω_1 is the resonant frequency for oscillator 1.

If $\mathbf{x_1}$ is driven by a time–dependent force which is proportional to the product of the amplitude $\mathbf{E}_o$ of the driver, or pump, and the amplitude $\mathbf{x}_2$ of the second oscillator, the equation of motion Eq. C.16 becomes:

$$\frac{d^2\mathbf{x_1}}{dt^2} + \omega_1^2\mathbf{x_1} = c_1\mathbf{x_2}\mathbf{E_o}, \tag{C.17}$$

where c_1 is a constant indicating the strength of coupling. A similar equation holds for $\mathbf{x_2}$ as follows:

$$\frac{d^2\mathbf{x_2}}{dt^2} + \omega_2^2\mathbf{x_2} = c_2\mathbf{x_1}\mathbf{E}_o \tag{C.18}$$

Now, let $\mathbf{x}_1 = \bar{\mathbf{x}}_1\cos\omega t$, $\mathbf{x}_2 = \bar{\mathbf{x}}_2\cos\omega' t$ and $\mathbf{E}_L = \mathbf{E}_o\cos\omega_o t$ substitute in Eq. C.18 , then we get:

$$(\omega_2^2 - \omega'^2)\bar{\mathbf{x}}_2\cos\omega' t = c_2\mathbf{E}_o\bar{\mathbf{x}}_1\cos\omega_o t\cos\omega t,$$

$$(\omega_2^2 - \omega'^2)\bar{\mathbf{x}}_2\cos\omega' t = c_2\mathbf{E}_o\bar{\mathbf{x}}_1\frac{1}{2}[\cos[(\omega_o + \omega)t] + \cos[(\omega_o - \omega)t]]. \tag{C.19}$$

The driving terms on the right can excite oscillators x_2 with frequencies as shown in Eq. C.20:

$$\omega' = \omega_o \pm \omega \tag{C.20}$$

In the absence of the nonlinear interactions, $\mathbf{x_2}$ can only have the frequency ω_2, so we must have $\omega' = \omega_2$. However, the driving terms can cause a frequency shift so that ω' is only approximately equal to ω_2. Furthermore, ω' can be complex, since there is damping (which has been neglected so far for simplicity), or there can be growth (if there is an instability). In either case, $\mathbf{x_2}$ is an oscillator with finite Q and can respond to a range of frequencies about ω_2. If ω is small, one can see from assumption Eq. C.20 that both choices for ω' may lie within the bandwidth of $\mathbf{x_2}$, and one must allow for the existence of the two oscillators $\mathbf{x_2}(\omega_o \pm \omega)$.

Now let $\mathbf{x_1} = \overline{\mathbf{x}}_1 \cos \omega"t$, and $\mathbf{x_2} = \overline{\mathbf{x}}_2 \cos[(\omega_o \pm \omega)]t$ insert into Eq. C.17:

$$(\omega_2^2 - \omega"^2)\overline{\mathbf{x}}_1 \cos \omega"t = c_1 \mathbf{E}_o \overline{\mathbf{x}}_2 \frac{1}{2}[\cos(\omega_o + (\omega_o \pm \omega)t) + \cos(\omega_o - (\omega_o \pm \omega)t)] = c_1 \mathbf{E}_o \overline{\mathbf{x}}_2 \frac{1}{2}[\cos(2\omega_o \pm \omega)t + \cos \omega t], \tag{C.21}$$

The driving terms can excite not only the original oscillation $\mathbf{x_1}(\omega)$, but also new frequencies $\omega" = 2\omega_o \pm \omega$. We shall consider the case $\mid \omega_o \mid \gg \mid \omega_1 \mid$, So that $2\omega_o \pm \omega$ lies outside the range of frequencies to which $\mathbf{x_1}$ can respond, and $\mathbf{x_1}(2\omega_o \pm \omega)$ can be neglected. We therefore have three oscillators $\mathbf{x_1}(\omega), \mathbf{x_1}(\omega_o + \omega)$ and $\mathbf{x_1}(\omega_o - \omega)$, which are coupled by Eqs. C.17 and C.18:

$$(\omega_1^2 - \omega^2)\mathbf{x_1}(\omega) - c_1 \mathbf{E}_o(\omega_o)[\mathbf{x_2}(\omega_o - \omega) + \mathbf{x_2}(\omega_o + \omega)] = 0, \tag{C.22}$$

$$[\omega_2^2 - (\omega_o - \omega)^2]\mathbf{x_2}(\omega_o - \omega) - c_2 \mathbf{E}_o(\omega_o)\mathbf{x_1}(\omega) = 0, \tag{C.23}$$

$$[\omega_2^2 - (\omega_o + \omega)^2]\mathbf{x_2}(\omega_o + \omega) - c_2 \mathbf{E}_o(\omega_o)\mathbf{x_1}(\omega) = 0, \tag{C.24}$$

The dispersion relation is given by setting the determinant of the coefficient equal to zero:

$$\begin{bmatrix} (\omega^2 - \omega_1^2) & c_1 \mathbf{E_o} & c_1 \mathbf{E_o} \\ c_2 \mathbf{E_o} & (\omega_o - \omega)^2 - \omega_2^2 & 0 \\ c_2 \mathbf{E_o} & 0 & (\omega_o + \omega)^2 - \omega_2^2 \end{bmatrix} = 0,$$

A solution with Im $\omega > 0$ would indicate instability.

By substitute the constants value according to our case (c_1 and c_2) into the above determinant we will get:

$$\begin{bmatrix} (\omega_{pe}^2 - \omega^2) & (iek/M_i)\mathbf{E}_o & (iek/M_i)\mathbf{E}_o \\ (-iek/M_i)\mathbf{E}_o & (\omega_o - \omega)^2 - \omega_2^2 & 0 \\ (-iek/M_i)\mathbf{E}_o & 0 & (\omega_o + \omega)^2 - \omega_2^2 \end{bmatrix} = 0,$$

by solving the above determinant we can obtain the following equation:

$$Q^3 - (2 + \widehat{\omega}_{pe}^2)Q^2 + (1 + 2\widehat{\omega}_{pe}^2 - 2\widehat{k}_{sp}^2 a_o^2 \frac{m_e}{M_i})Q - (\widehat{\omega}_{pe}^2 + 2\widehat{k}_{sp}^2 a_o^2 \frac{m_e}{M_i}) = 0. \qquad (C.25)$$

when $Q = \omega^2$, we are interesting in the imaginary part of ω which define the growth rate of the oscillating two stream instability $\omega = \omega_{real} + i\gamma_{ots}$. a_o is the laser parameter and it equals to $a_o = e\mathbf{E}_o/m_e c\omega_L = 0.85\lambda_L\sqrt{I_L}$ (I_L is the laser intensity in $[10^{18} \text{ W}/cm^2]$), $\widehat{k}_{sp} = k_{sp}/k_L$ is the normalized wavenumber of the surface plasma wave to the laser wavenumber, $\widehat{\omega}_{pe} = n_{inter}/n_{cr}$ is the normalized electron plasma frequency by the laser frequency , and $\left(\frac{m_e}{M_i}\right) = 0.0087$ is the electron to ion mass ratio.

Bibliography

[1] M. Hashida, Y. Miyasaka, Y. Ikuta, S. Tokita, and S. Sakabe. Crystal structures on a copper thin film with a surface of periodic self-organized nanostructures induced by femtosecond laser pulses. *Phys. Rev. B*, 83:235413, Jun 2011. doi: 10.1103/PhysRevB.83.235413.

[2] P. McKenna, D. Neely, R. Bingham, and D. Jaroszynski. Laser-plasma interactions and applications. *Springer, Heidelberg*, 2013. doi: doi.org/10.1007/978-3-319-00038-1.

[3] Two exhibits of Plasma Science and Technology sponsored by the Coalition for Plasma Science. the coalition for plasma science. *the House Office Buildings, Capitol Hill,Washington, District of Columbia.*, 1998. http://www.plasmas.org/what-are-plasmas.htm.

[4] F. Chen. Introduction to plasma physics and controlled fusion. *Springer International Publishing*, pages XII, 490, 2016. ISSN 1432-0630. doi: 10.1007/978-3-319-22309-4.

[5] A. Pukhov. Particle-in-cell codes for plasma-based particle acceleration. *CERN Yellow Reports*, 1:181, 2016.

[6] M. Shalaev. *Optical Properties of Nanostructured Random Media*. Topics in Applied Physics. Springer Berlin Heidelberg, 2003. ISBN 9783540449485.

[7] J. Thibault, Y. Derrien, T. Itina, R. Torres, T. Sarnet, and M. Sentis. Possible surface plasmon polariton excitation under femtosecond laser irradiation of silicon. *Applied Physics*, 114:083104, 2013. doi: 10.1063/1.4818433.

[8] M. Tsukamoto, K. Asuka, H. Nakano, M. Hashida, M. Katto, N. Abe, and M. Fujita. Periodic microstructures produced by femtosecond laser irradiation on titanium plate. *Vacuum*, 80:1346 – 1350, 2006. ISSN 0042-207X. doi: doi.org/10.1016/j.vacuum.2006.01.016. The 5th International Symposium on Applied Plasma Science, 26-30 September 2005, Hawaii, USA.

[9] A. Gouda, H. Sakagami, T. Ogata, M. Hashida, and S. Sakabe. The formation mechanism of the periodic nanograting structure by the weibel instability. *Applied Physics A*, 122:454, Mar 2016. ISSN 1432-0630. doi: 10.1007/s00339-016-9958-1.

[10] L. Gemini, M. Hashida, M. Shimizu, Y. Miyasaka, S. Inoue, S. Tokita, J. Limpouch, T. Mocek, and S. Sakabe. Periodic nanostructures self-formed on silicon and silicon carbide by femtosecond

laser irradiation. *Applied Physics A*, 117:49–54, Oct 2014. ISSN 1432-0630. doi: 10.1007/s00339-014-8502-4.

[11] S. Sakabe, M. Hashida, S. Tokita, S. Namba, and K. Okamuro. Mechanism for self-formation of periodic grating structures on a metal surface by a femtosecond laser pulse. *Phys. Rev. B*, 79: 033409, Jan 2009. doi: 10.1103/PhysRevB.79.033409.

[12] D. Ashkenasi, A. Rosenfeld, H. Varel, M. Wähmer, and E. Campbell. Laser processing of sapphire with picosecond and sub-picosecond pulses. *Applied Surface Science*, 120:65 – 80, 1997. ISSN 0169-4332. doi: doi.org/10.1016/S0169-4332(97)00218-3.

[13] A. Gouda, H. Sakagami, T. Ogata, M. Hashida, and S. Sakabea. Formation mechanism of a periodic nanograting structure by a surface plasma wave. *Plasma and Fusion Research*, 11: 2401071–2401071, 2016. doi: 10.1585/pfr.11.2401071.

[14] T. Jia, H. Chen, M. Huang, F. Zhao, J. Qiu, R. Li, Z. Xu, X. He, J. Zhang, and H. Kuroda. Formation of nanogratings on the surface of a znse crystal irradiated by femtosecond laser pulses. *Phys. Rev. B*, 72:125429, Sep 2005. doi: 10.1103/PhysRevB.72.125429.

[15] A. Ozkan, A. Malshe, T. Railkar, W. Brown, M. Shirk, and P. Molian. Femtosecond laser-induced periodic structure writing on diamond crystals and microclusters. *Applied Physics Letters*, 75: 3716–3718, 1999. doi: 10.1063/1.125439.

[16] J. Reif, F. Costache, M. Henyk, and V. Pandelov. Ripples revisited: non-classical morphology at the bottom of femtosecond laser ablation craters in transparent dielectrics. *Applied Surface Science*, 197-198:891 – 895, 2002. ISSN 0169-4332. doi: doi.org/10.1016/S0169-4332(02)00450-6. COLA'01 SI.

[17] N. Yasumaru and Hasida.M. International congress on laser advanced materials processing. *The Third Asian Pacific Laser Symposium (APLS2002), September 27-31, Osaka*, 2002.

[18] J. Bonse, H. Sturm, D. Schmidt, and W. Kautek. Chemical, morphological and accumulation phenomena in ultrashort-pulse laser ablation of tin in air. *Applied Physics A*, 71:657–665, Dec 2000. ISSN 1432-0630. doi: 10.1007/s003390000585.

[19] M. Hashida, M. Fujita, Y. Izawa, and F. Semerok. *Optical Properties of Nanostructured Random Media*, volume 4830 of *Topics in Applied Physics*. Laser Precision Microfabrication, Proceedings of SPIE, 2002.

[20] A. Vorobyev and C. Guo. Effects of nanostructure-covered femtosecond laser-induced periodic surface structures on optical absorptance of metals. *Applied Physics A*, 86:321–324, Mar 2007. doi: 10.1007/s00339-006-3800-0.

[21] T. Shinonaga, M. Tsukamoto, and G. Miyaji. Periodic nanostructures on titanium dioxide film produced using femtosecond laser with wavelengths of 388 nm and 775 nm. *Opt. Express*, 22: 14696–14704, Jun 2014. doi: 10.1364/OE.22.014696.

[22] T. Shinonaga, M. Tsukamoto, A. Nagai, K. Yamashita, T. Hanawa, N. Matsushita, G. Xie, and N. Abe. Cell spreading on titanium dioxide film formed and modified with aerosol beam and femtosecond laser. *Applied Surface Science*, 288:649 – 653, 2014. ISSN 0169-4332. doi: doi.org/10.1016/j.apsusc.2013.10.090.

[23] T. Kato and N. Abe. Laser commentary formation of metallic nano periodic structure by femtosecond laser and its application to friction reducing machine. *Rev. Laser Eng*, 37:510, 2009.

[24] N. Yasumaru, K. Miyazaki, and J. Kiuchi. Control of tribological properties of diamond-like carbon films with femtosecond-laser-induced nanostructuring. *Applied Surface Science*, 254:2364 – 2368, 2008. ISSN 0169-4332. doi: doi.org/10.1016/j.apsusc.2007.09.037.

[25] S. Matsumoto, A. Yane, S. Nakashima, M. Hashida, M. Fujita, Y. Goto, and S. Takahashi. A rapid flow mixer with 11-s mixing time microfabricated by a pulsed-laser ablation technique: Observation of a barrier-limited collapse in cytochrome c folding. *Journal of the American Chemical Society*, 129:3840–3841, 2007. doi: 10.1021/ja0660958.

[26] Y. Vorobyev and G. Chunlei. Direct femtosecond laser surface nano/microstructuring and its applications. *Laser & Photonics Reviews*, 7:385–407, August 2012. doi: 10.1002/lpor.201200017.

[27] M. Kawamoto, M. Hashida, Y. Miyasaka, M. Shimizu, M. Hata, S. Sakabe, and S. Tokita. Laser coloring of metal surface. *IEEJPn*, 2013:7–10, jul 2013.

[28] F. Floux. Nuclear fusion by laser radiation. *Nuclear Fusion*, 11:635, 1971.

[29] A. McKenzie. Lasers in surgery and medicine. *Physics in Medicine and Biology*, 29:619, 1984.

[30] G. Hancock. Lasers in photochemistry. *Journal of Photochemistry and Photobiology A: Chemistry*, 51:13 – 16, 1990. ISSN 1010-6030. doi: doi.org/10.1016/1010-6030(90)87035-A.

[31] D. Lichti, N. Pfeifer, and H. Maas. Isprs journal of photogrammetry and remote sensing theme issue "terrestrial laser scanning". *ISPRS Journal of Photogrammetry and Remote Sensing*, 63:1 – 3, 2008. ISSN 0924-2716. doi: 10.1016/j.isprsjprs.2007.10.002.

[32] M. Eghtedari, A. Oraevsky, A. Copland, A. Kotov, and A. Conjusteau. High sensitivity of in vivo detection of gold nanorods using a laser optoacoustic imaging system. *Nano Letters*, 7:1914–1918, 2007. doi: 10.1021/nl070557d.

[33] I. Langumir. The arrangement of electrons in atoms and molecules. *Journal of the American Chemical Society*, 41:861, 1919.

[34] H. Alfvén. Existence of electromagnetic-hydrodynamic waves. *Nature*, 4150:405–406, 1942. doi: 10.1038/150405d0.

[35] V. Smirnov. Tokamak foundation in ussr/russia 1950–1990. *Nuclear Fusion*, 50:014003, 2010.

[36] K. Miyamoto. Plasma physics and controlled nuclear fusion. *Springer*, 38:014003, 2005. doi: 10.1007/3-540-28097-9.

[37] G. Bonizzoni and E. Vassallo. Plasma physics and technology; industrial applications. *Vacuum*, 64, 2002. doi: 10.1016/S0042-207X(01)00341-4.

[38] M. Dawson. Particle simulation of plasmas. *Rev. Mod. Phys.*, 55:403–447, Apr 1983. doi: 10.1103/RevModPhys.55.403.

[39] F. Harlow. A machine calculation method for hydrodynamics problems. *Los Alamos Scientific Laboratory report LAMS-1956.*, 1955.

[40] H. Okuda. Nonphysical noises and instabilities in plasma simulation due to a spatial grid. *Journal of Computational Physics*, 10:475 – 486, 1972. ISSN 0021-9991. doi: doi.org/10.1016/0021-9991(72)90048-4.

[41] H. Sakagami and K. Mima. Fast ignition simulation with collective pic code. *Inertial Fusion Sciences and Applications*, 428, 2001. doi: 10.1051/0004-6361:20041882.

[42] S. Weibel. Spontaneously growing transverse waves in a plasma due to an anisotropic velocity distribution. *Phys. Rev. Lett.*, 2:83–84, Feb 1959. doi: 10.1103/PhysRevLett.2.83.

[43] H. Yoon. Relativistic weibel instability. *Physics of Plasmas*, 14:024504, 2007. doi: 10.1063/1.2646285.

[44] A. Grassi, M. Grech, F. Amiranoff, F. Pegoraro, A. Macchi, and C. Riconda. Electron weibel instability in relativistic counterstreaming plasmas with flow-aligned external magnetic fields. *Phys. Rev. E*, 95:023203, Feb 2017. doi: 10.1103/PhysRevE.95.023203.

[45] C. Huntington, F. Fiuza, J. Ross, A. Zylstra, R. Drake, D. Froula, G. Gregori, N. Kugland, C. Kuranz, M. Levy, C. K. Li, J. Meinecke, T. Morita, R. Petrasso, C. Plechaty, B. Remington, D. Ryutov, Y. Sakawa, A. Spitkovsky, H. Takabe, and H. Park. Observation of magnetic field generation via the weibel instability in interpenetrating plasma flows. *Nature Physics*, 11:023203, Jan 2015. doi: 10.1038/nphys3178.

[46] Y. Fujita, T. Kato, and N. Okabe. Magnetic field generation by the weibel instability at temperature gradients in collisionless plasmas. *Physics of Plasmas*, 13:122901, 2006. doi: 10.1063/1.2399467.

[47] A. Achterberg, J. Wiersma, and A. Norman. The weibel instability in relativistic plasmas - ii. nonlinear theory and stabilization mechanism. *A&A*, 475:19–36, 2007. doi: 10.1051/0004-6361:20065366. URL https://doi.org/10.1051/0004-6361:20065366.

[48] R. Schlickeiser and P. Shukla. Cosmological magnetic field generation by the weibel instability. *The Astrophysical Journal Letters*, 599:L57, 2003.

[49] J. Hill, M. Key, S. Hatchett, and R. Freeman. Beam-weibel filamentation instability in near-term and fast-ignition experiments. *Physics of Plasmas*, 12:082304, 2005. doi: 10.1063/1.1986988.

[50] J. Wiersma and A. Achterberg. Magnetic field generation in relativistic shocks - an early end of the exponential weibel instability in electron-proton plasmas. *Astronomy and Astrophysics*, 428: 365–371, 2004. doi: 10.1051/0004-6361:20041882.

[51] R. Kodama, P. Norreys, K. Mima, A. Dangor, R. Evans, H. Fujita, Y. Kitagawa, K. Krushelnick, T. Miyakoshi, N. Miyanaga, T. Norimatsu, S. Rose, T. Shozaki, K. Shigemori, A. Sunahara, M. Tampo, K. Tanaka, Y. Toyama, T. Yamanaka, and M. Zepf. Fast heating of ultrahigh-density plasma as a step towards laser fusion ignition. *Nature*, 412:798 Ep, 2001. doi: 10.1051/0004-6361: 20041882.

[52] Y. Furukawa, R. Sakata, K. Konishi, K. Ono, S. Matsuoka, K. Watanabe, S. Inoue, M. Hashida, and S. Sakabe. Demonstration of periodic nanostructure formation with less ablation by double-pulse laser irradiation on titanium. *Applied Physics Letters*, 108:264101, 2016. doi: 10.1063/1. 4955035.

[53] K. Okamuro, M. Hashida, Y. Miyasaka, Y. Ikuta, S. Tokita, and S. Sakabe. Laser fluence dependence of periodic grating structures formed on metal surfaces under femtosecond laser pulse irradiation. *Phys. Rev. B*, 82:165417, Oct 2010. doi: 10.1103/PhysRevB.82.165417.

[54] T. Derrien, R. Koter, J. Kruger, S. Hohm, A. Rosenfeld, and J. Bonse. Plasmonic formation mechanism of periodic 100-nm-structures upon femtosecond laser irradiation of silicon in water. *Journal of Applied Physics*, 116:074902, 2014. doi: 10.1063/1.4887808.

[55] M. Hashida, Y. Ikuta, Y. Miyasaka, S. Tokita, and S. Sakabe. Simple formula for the interspaces of periodic grating structures self-organized on metal surfaces by femtosecond laser ablation. *Applied Physics Letters*, 102:174106, 2013. doi: 10.1063/1.4803940.

[56] M. Hashida, T. Nishii, Y. Miyasaka, H. Sakagami, M. Shimizu, S. Inoue, and S. Sakabe. Orientation of periodic grating structures controlled by double-pulse irradiation. *Applied Physics A*, 122:484, Apr 2016. ISSN 1432-0630. doi: 10.1007/s00339-016-0011-1.

[57] U. Samir and N. Stone. The expansion of a plasma into a vacuum: Basic phenomena and processes and applications to space plasma physics. *Reviews of Geophysics*, 21:1631–1646, 1983. doi: 10.1029/RG021i007p01631.

[58] J. Zenneck. Über die fortpflanzung ebener elektromagnetischer wellen längs einer ebenen leiterfläche und ihre beziehung zur drahtlosen telegraphie. *Annalen der Physik*, 328:846–866, 1907. doi: 10.1002/andp.19073281003.

[59] L. Solymar and E. Shamonina. *Waves in Metamaterials*. Oxford University Press, Inc., New York, NY, USA, 2009. ISBN 0199215332, 9780199215331.

[60] J. Hermann, E. Axente, V. Craciun, A. Taleb, and F. Pelascini. Evaluation of pressure in a plasma produced by laser ablation of steel. *Spectrochimica Acta Part B: Atomic Spectroscopy*, 143:63 – 70, 2018. ISSN 0584-8547. doi: doi.org/10.1016/j.sab.2018.02.015.

[61] N. Iwata, S. Kojima, Y. Sentoku, M. Hata, and K. Mima. Plasma density limits for hole boring by intense laser pulses. *Nature Communications*, 9:623, 2018. doi: 10.1038/s41467-018-02829-5.

[62] H. Raether. Surface plasmons on smooth and rough surfaces and on gratings. *Springer, Heidelberg*, 1988. doi: 10.1007/BFb0048317.

[63] J. Hooper, A. Zalewski, and E. Watanabe. *Moving Average Crossovers*, chapter 4, pages 33–49. Wiley,B., 2014. ISBN 9781118657591. doi: 10.1002/9781118657591.ch4.